Genesis of oceanic oxide gabbros and gabbronorites during reactive melt migration at transform walls (Doldrums Megatransform System; 7-8°N Mid-Atlantic Ridge)

***Basch, V.[1,2], Sanfilippo, A.[1,2], Skolotnev, S.G.[3], Ferrando, C.[1], Muccini, F.[4], Palmiotto, C.[5], Peyve, A.A.[3], Ermolaev, B.V.[3], Okina, O.I.[3], Ligi, M.[5]**

[1] Dipartimento di Scienze della Terra e dell'Ambiente, Università di Pavia, Italy;
valentin.basch@gmail.com; alessio.sanfilippo@unipv.it; ottaferrando@gmail.com

[2] Istituto Geoscienze e Georisorse, Unità di Pavia, CNR, Pavia, Italy

[3] Geological Institute of the Russian Academy of Science, Moscow, Russia
sg_skol@mail.ru; apeyve@yandex.ru; ermolaev-bv@mail.ru; okina@bk.ru

[4] Istituto Nazionale Geofisica e Vulcanologia, Roma, Italy
filippo.muccini@ingv.it

[5] Istituto di Scienze Marine – CNR, Bologna, Italy
camilla.palmiotto@bo.ismar.cnr.it; marco.ligi@bo.ismar.cnr.it

Corresponding author:
* Valentin Basch
valentin.basch@gmail.com
Dipartimento di Scienze della Terra e dell'Ambiente, University of Pavia
Via Ferrata 1, 27100 Pavia, Italy

Abstract:

The Doldrums Megatransform System (~7-8°N, Mid-Atlantic Ridge) shows a complex architecture including four intra-transform ridge segments bounded by five active transform faults. Lower crustal rocks are exposed along the Doldrums and Vernadsky transform walls that bound the northernmost intra-transform ridge segment. The recovered gabbros are characterized by variably evolved chemical compositions, ranging from olivine gabbros to gabbronorites and oxide gabbros, and lack the most primitive gabbroic endmembers (troctolites, dunites). Notably, the numerous recovered gabbronorites show up to 20 vol% of coarse-grained orthopyroxene. Although covariations in mineral and bulk-rock chemical compositions of the olivine and oxide gabbros define trends of crystallization from a common parental melt, the gabbronorites show elevated light over heavy rare earth elements (LREE/HREE) ratios in both bulk-rock and mineral compositions. These features are not consistent with a petrological evolution driven solely by fractional crystallization, which cannot produce the preferential enrichments in highly incompatible elements documented in the orthopyroxene-bearing lithologies. We suggest that gabbronorites crystallized from evolved melts percolating and partly assimilating a pre-existing olivine gabbro matrix. Saturation in orthopyroxene and selective enrichments in LREE relative to M-HREE are both triggered by an increase in assimilated crystal mass, which ranges from negligible in the oxide-gabbros to abundant in the gabbronorites. This melt-rock reaction process has been related to lateral melt migration beneath ridge-transform intersections, where variably evolved melts injected from the peripheral parts of the melting region towards the transform zone may interact with a gabbroic crystal mush to form abundant oxide-bearing gabbronoritic associations.

Keywords: *Lower oceanic crust; Transform faults; Gabbronorites; Oxide gabbros; Lateral differentiation; Melt-rock interaction.*

1. INTRODUCTION

The architecture and composition of the oceanic crust accreted along the ~67000 km of modern oceanic ridges is highly variable (e.g., Chen, 1992; Carbotte and Sheirer, 2004; Cannat *et al.*, 2006, 2019; Dick *et al.*, 2006; White and Klein, 2014) and mainly dependent on the spreading rate and on the temperature of the upwelling mantle (e.g., Parmentier and Phipps Morgan, 1990; Bown and White, 1994; Langmuir and Forsyth, 2007). At slow spreading rates, magmatism is reduced and crustal accretion is partially accommodated by tectonic extension and exhumation of deep material

to the seafloor along oceanic detachments or transform faults (e.g., Cann *et al.*, 1997; Buck *et al.*, 2005; Tucholke *et al.*, 2008; Olive and Dublanchet, 2020; Bickert *et al.*, 2021). Between 0°N and 11°N, the Equatorial Atlantic is characterized by large-offset (>500 km) oceanic transform systems that displace the Mid-Atlantic Ridge axis for more than 3000 km in total. Conversely to the classical model of oceanic transform faults, defined as single narrow strike-slip zones offsetting two mid-ocean ridge segments (Wilson, 1965), these large-offset transform domains develop a broad (>100 km) lens-shaped zone of deformation and have been defined as "megatransform systems" (Ligi *et al.*, 2002). Furthermore, some of these equatorial long-offset transform systems are characterized by a multi-fault architecture (i.e., St-Paul and Doldrums megatransforms) and by the formation of magmatically active intra-transform ridges (ITR) developed within a lens-shaped shear zone (e.g., Bonatti, 1978; Sandwell and Smith, 1997; Hekinian *et al.*, 2000; Maia *et al.*, 2019; Skolotnev *et al.*, 2020). The development of ITRs and the active magmatism in these cold systems is thought to result from active mantle upwelling or from a transtensive regime resulting from changes in plate motion (Bonatti, 1978; Fox and Gallo, 1984; Maia *et al.*, 2016; Skolotnev *et al.*, 2020).

The long offset of megatransform systems results in a large age contrast between the actively spreading ridge axis and the aged lithosphere transposed on the opposite side of the active transform (Hekinian *et al.*, 2000; Ligi *et al.*, 2002, 2005; Maia *et al.*, 2016, 2019; Luo *et al.*, 2021). The juxtaposition of an active ridge axis with such a cold and thick lithosphere may cause a local decrease in the along-axis thermal gradient and degree of mantle melting approaching the transform, a cooling effect referred to as "cold edge effect" (e.g., Klein and Langmuir, 1987; Schilling *et al.*, 1995; Bonatti *et al.*, 1996a,b, 2001; Ligi *et al.*, 2002, 2005; Brunelli *et al.*, 2020).

An increased thickness of the lithosphere impedes shallow mantle melting (e.g., Langmuir & Forsyth, 2007), reduces melt productivity (e.g., Niu, 1997, 2021; Niu and Hekinian, 1997) and may favour interactions between migrating melts and mantle rocks (e.g., Collier and Kelemen, 2010; Dick *et al.*, 2010; Warren and Shimizu, 2010). Notably, dissolution-precipitation reactions occurring in the mantle (e.g., Dijkstra *et al.*, 2003; Suhr *et al.*, 2008; Sanfilippo *et al.*, 2014; Basch *et al.*, 2018, 2019a, 2019b; Rampone *et al.*, 2020) can modify the composition of the percolating melts, leading to specific trace element enrichments and to modifications in the crystallization order and in the liquid and crystal lines of descent (Collier and Kelemen, 2010; Sanfilippo *et al.*, 2016; Basch *et al.*, 2019b). Several studies evidenced that interactions between a melt and a pre-existing matrix may also occur in oceanic magma chambers, with a strong impact on the composition of the newly formed minerals (e.g., Coogan *et al.*, 2000; Lissenberg and Dick, 2008; Lissenberg *et al.*, 2013; Sanfilippo *et al.*, 2020; Ferrando *et al.*, 2021a, 2021b). If a general agreement exists that

melt-mush reactions may contribute to the chemical evolution of the lower oceanic crust (Lissenberg and MacLeod, 2016; Lissenberg *et al.*, 2019; Boulanger *et al.*, 2020; Sanfilippo *et al.*, 2020; Ferrando *et al.*, 2021a,b), to what extent these processes may be enhanced by the thickening of the lithosphere, and/or by melt focusing related to the tectonic activity at the transform, is still a matter of debate (see Brunelli *et al.*, 2020)

In this contribution, we report bulk-rock and mineral major and trace element compositions of gabbros and associated basalts recovered in the northern part of the Doldrums Megatransform System (7-8°N, Mid-Atlantic Ridge). There, the gabbroic crust sampled at the transform walls is characterized by chemically evolved compositions and shows the unexpected occurrence of orthopyroxene as an early magmatic phase. We relate these distinct modal and chemical features to the context of long-offset transform domains, and suggest that lateral differentiation, together with melt-mush reactions during melt transport, led to the distinct abundance of oxide gabbros and gabbronorites along transform walls.

2. GEOLOGICAL SETTING

In the Equatorial region of the Atlantic Ocean, the Mid-Atlantic Ridge (MAR) is characterized by short ridge segments (<200 km), separated by long-offset transform faults and megatransform systems, the largest of which are: Romanche (~950 km; e.g., Bonatti *et al.*, 1994; Searle *et al.*, 1994; Ligi *et al.*, 2002); Doldrums (total offset of ~630 km; Skolotnev *et al.*, 2020; Sani *et al.*, 2020); St-Paul (total offset of ~580 km; e.g., Hekinian *et al.*, 2000) and Vema (~310 km; e.g., Bonatti *et al.*, 2003, 2005; Cipriani *et al.*, 2009; Brunelli *et al.*, 2020). Together, these transform systems offset the Mid-Atlantic Ridge by more than 3000 km (from 16°W to 44°W) between 0°N and 11°N.

The Doldrums transform system is located at 7-8°N in the Equatorial Atlantic and offsets the Mid-Atlantic Ridge by 630 km from 34°W to 39.5°W. Similar to other megatransform systems (e.g., Hekinian *et al.*, 2000; Ligi *et al.*, 2002; Maia *et al.*, 2019), it is characterized by a multi-fault 110 km-wide lens-shaped deformed domain. Recent bathymetric surveys (e.g., Skolotnev *et al.*, 2020) highlighted its morphological complexity, with the occurrence of 4 ITR segments delimited by 5 active transform faults, namely the Doldrums, Vernadsky, 7.4°N, Pushcharovsky and Bogdanov transforms (Fig. 1a). The offsets of the single transform faults increase northwards, reaching 145 km and 177km along the Vernadsky and Doldrums transform faults, respectively. Considering half-spreading rates of 15 mm/yr (Cande *et al.*, 1988), the age offset across these transform faults is ~10 Ma and ~12 Ma, respectively (Skolotnev *et al.*, 2020).

Dredge sampling along the Doldrums transform system was carried out with *R/V Akademik Nikolaj Strakhov* during two expeditions in the late 1980s' (S06 in 1987-1988 and S09 in 1990; Pushcharovsky *et al.*, 1991, 1992) and more recently in 2019, in the frame of a collaborative Russian-Italian Research Program (S45; Skolotnev *et al.*, 2020). Fifty-two dredges in total recovered exclusively fresh basalts along the ITR-2, ITR-3 and ITR-4, whereas peridotitic and gabbroic rocks were sampled along the Vernadsky and Doldrums transform walls and from bathymetric highs located on the ITR-1 rift shoulders (Fig. 1b; Skolotnev *et al.*, 2020). In this study, we focus on gabbroic rocks and associated basalts sampled in 8 dredge hauls deployed along the two transforms, as reported in Figure 1b.

3. BATHYMETRY AND SAMPLING

The studied samples have all been recovered in the northernmost part of the Doldrums Megatransform System, within the ITR-1 domain. From north to south, the main bathymetric features of the studied area are: *i)* the Doldrums transform valley, *ii)* the ITR-1 segment, *iii)* OCC 8.1°N, *iv)* the Vernadsky transform valley and *v)* Seamount Peyve (Fig. 1b).

3.1. Doldrums transform and ITR-1

The Doldrums transform offsets the MAR West and ITR-1 segments by 177 km. Within the Doldrums transform valley, a 130 km-long and 1500 m-high median ridge separates the active transform valley to the south from an inactive transform valley to the north. The median ridge is in continuity with the eastern shoulder of the ITR-1 (Fig. 1b).

The ITR-1 is a 55-kilometre-long ridge segment characterized by a symmetrical rift valley and a continuous axial neovolcanic zone (Supplementary Figure S1a). Although single volcanic edifices can be observed at the northern extremity of the neovolcanic ridge axis, the central part of the rift valley is shallower (4200-4400 metre depth), and the volcanic activity appears more intense.

On the western shoulder of the ITR-1 valley, at the intersection between the ITR-1 and the Doldrums transform valley, a 25 km-long and 20 km-wide inner corner high previously described as an Oceanic Core Complex (OCC 8.1°N; Skolotnev *et al.*, 2020) shows a dome-shaped structure and reaches 1600m depth (Fig. S1a). It is characterized by gentle slopes plunging 12° towards the east and the west (Fig. S1b) and its surface presents corrugations extending perpendicular to the rift valley (Fig. S1a).

Sampling along the Doldrums transform recovered variably tectonized gabbros and peridotites from the northern and southern wall of the active transform valley (Pushcharovsky *et al.*, 1991, 1992; Skolotnev *et al.*, 2020). This study includes 9 gabbroic samples from the Doldrums transform

walls (dredges S09-69, S09-76 and S09-81; Fig. 1b), namely 1 olivine gabbro, 5 gabbros, 2 gabbronorites and 1 oxide gabbro (Supplementary Table S1).

3.3. Vernadsky transform and Peyve Seamount

The Vernadsky transform offsets the ITR-1 and ITR-2 segments by 145 km. It is characterized by progressively shallower depths moving eastward from the nodal basin (6040 m; 38°W) along the active transform valley (Supplementary Figure S2a). The southern wall of the transform gently plunges into the valley (5-15°; Fig. S2b,c,d), whereas the northern wall of the transform is characterized by steep slopes (20-30°; Fig. S2b,c,d). The latter transform wall is also characterized by the occurrence of a large structural high named Peyve Seamount (from 37°50'W to 37°33'W) and of a well-developed volcanic fabric deepening into the transform valley (from 37°33'W to 37°20'W) (Fig. S2a).

Peyve Seamount, located 25 km to the east with respect to the ITR-1 rift valley, is a 33 km-long and 8 km-wide prominent bathymetric high elongated along the Vernadsky transform wall. It is the shallowest portion of the entire Doldrums Megatransform System, rising 3700 m above the transform valley floor and reaching a minimum depth of 1033 m (Fig. 2a). It is characterized by a flat top, abruptly dipping between 21 and 34° into steep flanks on all sides (Fig. 2b,c,d). This bathymetric high deepens to the north into a well-developed volcanic fabric characterized by a succession of ridges and valleys parallel to the ITR-1 axis (Fig. 2a).

The sampling of the Vernadsky transform wall was deployed from the Vernadsky transform valley to the top of Peyve Seamount (Fig. 1b; Fig. 2d). Peridotites, variably evolved gabbros (Fig. 2e) and minor basalts were recovered (Pushcharovsky *et al.*, 1991, 1992; Skolotnev *et al.*, 2020). This study includes 45 samples from the northern wall of the Vernadsky transform (dredges S06-64, S09-61, S45-07, S45-08, S45-10; Fig. 1b), namely 6 olivine gabbros, 6 gabbros, 10 gabbronorites, 15 oxide gabbros and 8 basalts (Supplementary Table S1).

4. PETROGRAPHY

The studied gabbroic rocks range from olivine gabbros to gabbros *sensu stricto*, olivine gabbronorites, gabbronorites, oxide gabbronorites and oxide gabbros (Fig. 2e; Fig. 3). Most of the studied gabbros have been sampled from the southern slope of the Peyve Seamount, where the high number and density of dredges deployed (Fig. 2d) along the transform valley likely allowed for a representative sampling of this portion of oceanic crust.

Olivine gabbro shows a hypidiomorphic texture of millimetric olivine (5-10 vol%), plagioclase (50-55 vol%), clinopyroxene (35-40 vol%) and rare brown to dark green amphibole occurring at clinopyroxene rims (Fig. 4a,b). A single 500µm euhedral orthopyroxene crystal was found in an olivine gabbro sample (S45-7-2; Fig. 4a). Anhedral olivine commonly show irregular and lobate contacts with large plagioclase crystals (Fig. 4b). In places, plagioclase shows evidence of plastic deformation, with the occurrence of mechanical twins and undulose extinctions (Fig. 4b). Euhedral plagioclase laths are commonly found included in subhedral to anhedral clinopyroxene (Fig. 4b).

Gabbro sensu stricto shows a hypidiomorphic texture of millimetric plagioclase (50-55 vol%) and clinopyroxene (45-50 vol%) (Fig. 4c). Some samples show aggregates of 200-500 µm-size plagioclase neoblasts with equilibrated textures, likely resulting from partial recrystallization of plagioclase (Fig. 4c).

Gabbronorite, here referred to all samples containing more than 5 volume percent of orthopyroxene, range from olivine gabbronorite to gabbronorite and oxide gabbronorite. All samples are characterized by a hypidiomorphic texture of millimetric plagioclase (50-60 vol%), clinopyroxene (20-30 vol%) and orthopyroxene (5-14 vol%) (Fig. 5a), but olivine gabbronorite shows the occurrence of olivine (5-8 vol%) and oxide gabbronorite the presence of Fe-Ti oxides (8-10 vol%) and brown amphibole (3-5 vol%) (Fig. 5b). Orthopyroxene occurs as millimetric to centimetric euhedral crystals in all gabbronoritic samples (Fig. 5a) and Fe-Ti oxides are interstitial in the oxide gabbronorite (Fig. 5b). Orthopyroxene and clinopyroxene crystals are mostly undeformed (Fig. 5a), whereas aggregates of 200-500 µm-size plagioclase neoblasts found at the contact with deformed plagioclase suggest deformation and partial recrystallization of plagioclase crystals (Fig. 5a,b). Notably, a sharp contact between gabbronorite and oxide gabbronorite has been sampled (S45-7-4B) and shows an irregular shape (Fig. S1a).

Oxide gabbro shows a hypidiomorphic texture of millimetric plagioclase (50-60 vol%), clinopyroxene (25-30 vol%), Fe-Ti oxides (5-15 vol%) and minor orthopyroxene (0-5 vol%) and brown to dark green amphibole (3-5 vol%) (Fig. 5c,d). Fe-Ti oxide occurs as interstitial crystals around euhedral plagioclase and subhedral clinopyroxene (Fig. 5c). Variations in grain size are observed at the scale of the thin section (S45-7-6A), between coarse-grained intervals presenting a weak foliation of deformed plagioclase laths, and fine-grained granular domains (Fig. 5d). The fine-grained domains enclose partially corroded coarse-grained plagioclase laths similar to the crystals forming the coarse-grained oxide gabbro.

5. ANALYTICAL METHODS

5.1. Bulk-rock chemical compositions

Bulk-rock major element analyses were performed on 54 samples recovered in the ITR-1 domain during the S06, S09 and S45 campaigns (Supplementary Table S1), namely 45 samples from the Vernadsky transform wall, and 9 samples from the Doldrums transform walls (Fig. 1b). Internal portions of all gabbroic and basaltic rocks were crushed and pulverized in a tungsten carbide swing mill and analyzed at the Laboratory of chemical and analytical research of the Geological Institute, Russian Academy of Science (Moscow, Russia), using an S4 Pioneer X-Ray Fluorescence spectrometer (Bruker, Germany). Loss on Ignition (LOI) was defined by measuring the difference in mass of the powdered samples before and after being heated to 950°C for twelve hours in a chamber furnace. The Fe_2O_3 content of the whole-rock analyses has been converted to FeO using a conversion factor of 0.8998.

Bulk-rock trace element contents were determined on 26 samples recovered from the Vernadsky transform wall and 6 samples from the Doldrums transform walls (Supplementary Table S1). Powdered samples were dissolved using a mixture of hydrofluoric and nitric acids. The solution was subsequently evaporated with perchloric, boric and nitric acids and transferred into separate flasks using 3 % nitric acid and In as an internal standard at the Laboratory of chemical and analytical research of the Geological Institute, Russian Academy of Science (Moscow, Russia). Sample analyses were carried out using an Element2 mass spectrometer (Thermo Fisher Scientific GmbH, Germany). Total analytical errors of the element analyses are within 10 %.

5.2. Mineral chemical compositions

Mineral major and trace element analyses were performed on 11 samples recovered from the southern slope of Peyve Seamount during Expedition S45, namely 2 olivine gabbros, 1 gabbro, 5 gabbronorites and 3 oxide gabbros.

Major element compositions (SiO_2, TiO_2, Al_2O_3, Cr_2O_3, FeO, MgO, MnO, CaO, NiO, Na_2O, K_2O, Cl) of plagioclase, clinopyroxene, orthopyroxene, olivine, amphibole and Fe-Ti oxides were analysed by a JEOL JXA 8200 Superprobe equipped with five wavelength-dispersive (WDS) spectrometers, an energy dispersive (EDS) spectrometer, and a cathodoluminescence detector operating at the Dipartimento di Scienze della Terra, University of Milano, Italy. The analyses of all elements were performed with a 1-micron spot size, 30-seconds counting time at an accelerating potential of 15 kV and a beam current of 15 nA.

Trace element compositions of clinopyroxene, plagioclase, orthopyroxene and amphibole were determined by Laser Ablation-Inductively Coupled Plasma-Mass Spectrometry (LA-ICP-MS) at CNR, Istituto di Geoscienze e Georisorse (Unità di Pavia). We used a PerkinElmer SCIEX ELAN DRC-e quadrupole mass spectrometer coupled with an UP213 deep-UV YAG Laser Ablation System (New Wave Research, Inc.). Laser (213nm wavelength) spot size was set to 100µm and the ablation frequency to 10 Hz, with a fluence of ~9.5 J/cm2. Helium was used as the carrier gas and was mixed with Ar downstream from the ablation cell. Data reduction was performed using the GLITTER software. NIST SRM 612 synthetic glass was used as the external standard, and CaO and SiO_2 concentrations previously measured by EPMA were used as the internal standard. The precision and accuracy of the trace element concentrations were assessed by repeated analyses of the BCR2-g standard and were better than ±7% and ±10%, respectively.

6. RESULTS

6.1. Bulk-rock major and trace element compositions

The studied gabbros define a wide range of bulk-rock compositions (Supplementary Table S1), from high Mg-numbers (Mg# = Mg/[Mg+Fe] mol%) in olivine gabbros, gabbros and gabbronorites (Mg# = 56.37-79.81) to lower Mg-numbers in oxide gabbros (Mg# = 18.30-61.22) (Fig. 6a). Ca-numbers (Ca# = Ca/[Ca+Na] mol%) also show higher values for olivine gabbros and slightly decrease from gabbros to gabbronorites and oxide gabbros (Ca# ranging from 52.4 to 80.4; Fig. 6a). The analysed samples define a compositional trend characterized by decreasing MgO and increasing FeO contents (Fig. 6b) from olivine gabbros to gabbros, gabbronorites, and oxide gabbros. Similarly, at decreasing MgO contents, the bulk-rock compositions of olivine gabbros, gabbros and gabbronorites show a progressive increase in SiO_2 (Fig. 7a), CaO (Fig. 7b), Al_2O_3 (Fig. 7c), TiO_2 (Fig. 7d) and Na_2O (Fig. 7e). Oxide gabbros show a distinct compositional trend at decreasing MgO contents, in continuity with the most evolved gabbros and gabbronorites; they show decreasing contents of SiO_2 (Fig. 7a), CaO (Fig. 7b), Al_2O_3 (Fig. 7c) and a strong increase in TiO_2 (Fig. 7d) and Na_2O contents (Fig. 7e). All gabbroic samples show relatively homogeneous CaO/Al_2O_3 ratios (Fig. 7f). The bulk-rock compositions of the studied samples fall within the composition field of the gabbros drilled at the Atlantis Massif in the Mid-Atlantic Ridge (Godard *et al.*, 2009) and at the Atlantis Bank in the Southwest Indian Ridge (Dick *et al.*, 2000) (Fig. 6, Fig. 7). Notably, the compositional field of the gabbros reported from the Atlantis Massif extends to more primitive compositions than the Atlantis Bank and the studied samples (i.e., higher Mg# and MgO contents; Fig. 6a,b). As a mean of comparing the bulk composition of the gabbroic crust exposed at

the transform wall with that of Hole 1309D drilled in the core of the Atlantis Massif (Godard *et al.*, 2009) and Hole 735B drilled in the core of the Atlantis Bank (Dick *et al.*, 2000), we estimated a bulk composition of the crustal section exposed along the Vernadsky transform wall (referred to as "bulk Vernadsky" in Figure 6). The latter was calculated based on the weighted average of all the gabbroic samples recovered from the eight dredges deployed along a single transect from the base of the transform wall to the top of the Peyve Seamount (Fig. 2d). We defined the bulk-rock chemical composition of each lithology, that have then been scaled to the mass fractions of the dredged samples (Fig. 2e; 28 wt% olivine gabbros, 13 wt% gabbros; 10 wt% gabbronorites, 49 wt% oxide gabbros; see Skolotnev *et al.*, 2020). Although the recovered samples are likely not representative of the whole Peyve Seamount, we are confident that the calculated bulk Vernadsky provides a first-order estimate of the composition of the gabbroic crust formed at the ridge-transform intersection. According to this rough estimate, the bulk Vernadsky transform wall (orange star in Fig. 6) is characterized by more evolved compositions than the calculated bulk composition of both Hole 1309D gabbros (light grey star in Fig. 6) and Hole 735B (dark grey star in Fig. 6), extending towards lower Mg- and Ca-numbers (Fig. 6a), lower MgO and higher FeO contents (Fig. 6b).

The studied gabbroic rocks also show large bulk-rock incompatible trace element compositional variability (Fig. 8; Supplementary Table S1). REE concentrations increase from olivine gabbros to gabbros, gabbronorites and oxide gabbros (up to Yb_N = 37.40; $_N$ = normalized to C1-chondrite after Sun & McDonough, 1989) (Fig. 8a,b). Olivine gabbros and gabbros show the lowest LREE/HREE fractionation (Fig. 8a), whereas more variable LREE/HREE fractionation is observed in gabbronorites (Fig. 8b) and oxide gabbros (Fig. 8a). The most evolved gabbronorites are characterized by a negative Eu anomaly, whereas olivine gabbros, gabbros and oxide gabbros are characterized by positive Eu anomalies (Fig. 8a,b). Olivine gabbros, gabbros and gabbronorites show negative Ti, Zr and Hf anomalies, whereas oxide gabbros show positive anomalies for these elements (Fig. 8c,d).

The basalts recovered from Peyve Seamount (Supplementary Table S1) are characterized by variable major element bulk-rock compositions, from primitive to relatively evolved compositions (Mg# = 50.72-68.74; Ca# = 58.08-68.87). They show relatively flat REE patterns at low REE contents and no anomalies in highly incompatible elements respect to N-MORB compositions (after Workman and Hart, 2005).

6.2. Mineral major and trace element compositions

The mineral major element compositions of the gabbros from the Vernadsky transform wall are consistent with those of the gabbros drilled at the Atlantis Massif along the Mid-Atlantic Ridge (Fig. 9; Miller *et al.*, 2009) and at the Atlantis Bank along the Southwest Indian Ridge (Fig. 9; Dick *et al.*, 2002).

Clinopyroxene (Supplementary Table S2) shows compositional trends defined by a positive correlation between the Mg-number and the Al_2O_3 content (Fig. 9a), both higher in olivine gabbros and gabbros (Mg# = 78.69-81.32) respect to gabbronorites and oxide gabbros (Mg# = 57.08-78.07). TiO_2 contents initially increase at decreasing Mg-number, before decreasing at lower Mg-numbers (Fig. 9b). Accordingly, clinopyroxene analysed in olivine gabbros and gabbros show higher TiO_2 contents than the ones analysed in Fe-Ti oxide-bearing lithologies, i.e., the oxide gabbronorites and the oxide gabbros, as the result of Fe-Ti oxides co-saturation (e.g., Dick *et al.*, 2002; Botcharnikov *et al.*, 2008).

Clinopyroxene shows strong trace element compositional variations mirroring the bulk-rock compositional variability (Fig. 10a). Low REE concentrations and low LREE/MREE ratios characterize the olivine gabbros and gabbros, whereas high REE concentrations and relatively low LREE/MREE ratios characterize clinopyroxene within the oxide gabbros (up to Yb_N = 129.91). Clinopyroxene in gabbronorites is distinct from those in the other lithologies, with higher LREE/MREE ratios (Fig. 10a). Clinopyroxene from the analyzed gabbroic rocks shows negative Eu and Sr anomalies, which become increasingly marked at higher REE contents. Additionally, clinopyroxene within gabbronorites also displays strong negative Ti anomalies (Fig. 10b) and some show negligible to slightly positive Zr-Hf anomalies, contrasting with the strongly negative Zr-Hf anomalies characterizing clinopyroxene analysed within olivine gabbros, gabbros and oxide gabbros (Fig. 10b).

Plagioclase (Supplementary Table S3) shows decreasing Anorthite contents (An = Ca/[Ca+Na] mol%) at decreasing clinopyroxene Mg-numbers (Fig. 9c) and increasing K_2O contents (Fig. 9d), from olivine gabbros to gabbros, gabbronorites and oxide gabbros (An varying from 70.01 to 20.01 mol%).

Plagioclase within the olivine gabbros shows low REE abundances, whereas REE concentrations are higher and more variable in gabbros, gabbronorites and oxide gabbros (up to Ce_N = 11.07; Fig. 10c). Plagioclase within all lithologies show positive Eu, Sr and Ba anomalies (Fig. 10d).

Orthopyroxene (Supplementary Table S4) shows a positive correlation between Mg-numbers, Al_2O_3 (Fig. 9e) and TiO_2 contents (Fig. 9f), progressively decreasing from olivine gabbros to gabbronorites and oxide gabbros (Mg# varying from 73.72 to 44.38 mol%).

The orthopyroxene analysed within the olivine gabbro displays lower REE concentrations than the orthopyroxene analysed within the gabbronorites and oxide gabbros (Fig. 10e). Although variable, some orthopyroxenes analysed in the gabbronorites show enrichments in Zr and Hf relative to neighbouring elements (Fig. 10f).

Amphibole (Supplementary Table S5) is characterized by low silica contents and high TiO_2, alkaline (Na+K) and alumina contents and is classified as pargasite to edenite (classification after Leake *et al.*, 1997). Pargasite is mainly found as interstitial phases, although euhedral crystals locally occur within the oxide gabbros.

Pargasitic amphibole trace element compositions show increasing REE contents (Fig. 10g) from olivine gabbros to oxide gabbros and gabbronorites (up to $Yb_N = 59.32$). Notably, amphibole within the gabbronorites shows higher LREE/MREE ratios than amphibole analysed in the olivine and oxide gabbros (Fig. 10g). Within the gabbronorites, amphibole also shows positive anomalies in Nb, Ta, Zr and Hf (Fig. 10h), contrasting with the negative Zr-Hf anomalies characterizing amphibole analysed within olivine gabbros and oxide gabbros.

Olivine (Supplementary Table S6) shows relatively low Mg-numbers and NiO contents in olivine gabbros and olivine-bearing gabbronorites (Mg# = 68.80-72.73; NiO = 0.01-0.13 wt%).

7. DISCUSSION

7.1. Composition of the oceanic crust exposed at oceanic transform walls

Extensive sampling of the Doldrums Megatransform System allowed the recovery of numerous gabbroic rocks from the ITR-1 domain, and more specifically from the edges of the ITR segment (Fig. 1b). The investigated gabbros were recovered in 3 dredges from the walls of the Doldrums transform valley (Fig. 1b) and 5 dredges from the Vernadsky transform valley that were deployed on the southern slope of Seamount Peyve (Fig. 1b; Fig. 2d), sampling a transect of the Vernadsky transform wall (Fig. 1b).

The bulk-rock major element compositions of the studied gabbros define crystal lines of descent similar to those of the lower crustal sequence of IODP Site U1309 at the Atlantis Massif (30°N, Mid-Atlantic Ridge; Godard *et al.*, 2009) (Fig. 6; Fig. 7), although we emphasize important differences in the proportion of the gabbroic lithologies. Unlike the rocks drilled in the central part of the Atlantis Massif OCC (IODP Site U1309), 20 km from the transform valley (Godard *et al.*, 2009), the gabbros collected along the walls of the Doldrums and Vernadsky transforms lack the most primitive lithologic endmembers such as dunites and troctolites (Fig. 6). They are characterized by a large proportion of chemically evolved oxide-bearing gabbros and gabbronorites

(49 wt% at Peyve Seamount; Fig. 2e; Fig. 6; Fig. 7). Based on *MELTS* calculations, Sanfilippo *et al.* (2019) quantified that oxide gabbros are expected to represent less than ~20 wt% of the gabbros fractionated by a primitive MORB melt. The excess in Fe-Ti oxides within the gabbros sampled along the Vernadsky and Doldrums transform walls points to an overall evolved composition of the gabbroic layer, that may in turn suggest some extent of fractionation of the parental melts prior to their emplacement within the transform domain.

In the vicinity of a ridge-transform intersection, seafloor spreading is mainly accommodated by tectonic extension; the lithosphere is thicker and melt production is scarce (e.g., Hooft *et al.*, 2000; Behn and Ito, 2008; Bai and Montési, 2015). Additionally, the cold edge effect induced by large-offset transform faults can lead to further thickening of the oceanic lithosphere and a progressive decrease in melt productivity along the ridge axis (Ligi *et al.*, 2002, 2005). In such a cold oceanic environment characterized by a thick lithosphere, melt production may cease at high pressure (~8-10 kbar; e.g., Langmuir and Forsyth, 2007) and melts need to migrate for greater distances before pooling in shallow magma chambers to form the gabbroic crust (e.g., Niu, 2021). Therefore, one possibility to explain the distinctly evolved composition of the gabbroic crust in this region is that primary melts could have undergone chemical evolution during their migration through a thick lithosphere, at depths greater than the exposed gabbroic crust (< 2 kbar; "*High-pressure differentiation*" in Fig. 11; e.g., Warren and Shimizu, 2010; Bennett *et al.*, 2019). Yet, the basalts recovered on top of Peyve Seamount show primitive compositions (Mg# > 67; Supplementary Table S1) indicating that melts produced beneath the transform wall experienced limited differentiation during their migration from the source region. Additionally, high melt supply along the entire ITR-1 is evidenced by a well-developed volcanic fabric immediately north of Peyve Seamount and south of the Doldrums transform wall (Fig. 1b; Fig. 4a). We therefore argue that the juxtaposition of the ridge axis with the ~12 and ~10 Ma lithosphere across the Doldrums and Vernadsky transforms, respectively, did not strongly reduce melt production in the underlying mantle. We thus exclude that primary melts might have extensively fractionated during migration through a thick lithosphere before forming the gabbroic crust in this transform domain.

Alternatively, the abundance of Fe-Ti oxides in the gabbroic crust sampled at the transform walls can be explained by processes of lateral differentiation (e.g., Dick *et al.*, 2019; Brunelli *et al.*, 2020). This process implies that melts produced in the most peripheral parts of the melting region beneath a ridge segment can be focused towards the actively deforming lithosphere in the vicinity of the ridge-transform intersection and be emplaced along the transform domain ("*Lateral differentiation*" in Fig. 11; see Brunelli *et al.*, 2020). These melts experience extensive fractionation prior to their intrusion into the transform wall, producing a lower oceanic crust distinctly enriched

in Fe-Ti oxides. In the following, we will show that such a process of lateral melt migration is a common feature, and when locally associated with melt-rock reactions, can account for the composition of the gabbroic crust sampled at the Doldrums and Vernadsky transform walls.

7.2. Lateral melt differentiation as a common process at slow-spreading transform faults

An evolved composition of the gabbroic crust sampled along transform walls has been previously documented in other slow- to ultraslow-spreading environments worldwide, such as the Atlantis Bank (e.g., Dick *et al.*, 2019) and the Vema Lithospheric Section (Brunelli *et al.*, 2020). At the Atlantis Bank along the Southwest Indian Ridge, extensive dredging, diving, and drilling evidenced a compositional zonation both laterally and vertically, with a vast majority of olivine gabbros characterizing the centre of the gabbroic body (i.e., ODP Hole 735B and IODP Hole U1473A) and a high proportion of oxide gabbros towards the exterior (e.g., Dick *et al.*, 2000, 2002, 2019; MacLeod *et al.*, 2017). This lithological zonation is believed to result from progressive differentiation of the melts away from the core of the Atlantis Bank gabbroic massif, where melts were transported from the mantle to the crust (see Dick *et al.*, 2019). Thus, the evolved composition of the gabbroic crust sampled along the Atlantis II transform wall results from processes of lateral melt migration and differentiation. Along the Vema Fracture Zone, extensive sampling provided documentation of a complete section of oceanic lithosphere, from residual peridotites to intrusive gabbros and extrusive volcanics (Auzende *et al.*, 1989; Cannat *et al.*, 1991; Brunelli *et al.*, 2020). The gabbros exposed there are strongly evolved, showing widespread occurrence of Fe-Ti oxides and apatite. Brunelli *et al.* (2020) interpreted the excess in oxide gabbros as the result of lateral differentiation of melts that migrated from the magmatically robust segment centre to the magma-poor ridge-transform intersection. Therefore, the evolved composition of the gabbroic crust sampled along the Atlantis II and Vema transform appears to be a direct consequence of lateral differentiation processes and the scarce magmatism in the vicinity of the transform zone, similar to what we document at the ITR-1 (Fig. 11). We emphasize, however, that such processes of lateral melt migration most likely occurred only at segment edges; the well-documented Atlantis Bank (e.g., Dick *et al.*, 2019) allows to constrain the extent of such processes to few tens of kilometers from the transform at most. This in turn implies that the melts migrating laterally do not necessarily originate at the centre of a ridge segment, as it was inferred by Brunelli *et al.* (2020), but simply from magmatically productive peripheral portions of the melting region, close to the transform zone (Fig. 11).

Additionally, numerous accounts of evolved oxide-rich gabbroic crust sampled along transform walls have been documented in slow-spreading environments worldwide, although not investigated

in detail, namely along: *i)* Andrew Bain (Southwest Indian Ridge; Takeuchi *et al.*, 2010); *ii)* Mado Megamullion (Philippine Sea; Basch *et al.*, 2020; Akizawa *et al.*, 2021); *iii)* Atlantis (Atlantis Massif, Mid-Atlantic Ridge, e.g., Blackman *et al.*, 2002, 2011; Boschi *et al.*, 2006; Karson *et al.*, 2006), and i*v)* Kane (Mid-Atlantic Ridge, e.g., Mével *et al.*, 1991; Auzende *et al.*, 1994; Dick *et al.*, 2008). Lateral melt migration and formation of gabbroic crust with anomalously evolved composition therefore appears to be a common characteristic of the lower oceanic crust sampled along transform walls at slow-spreading ridges (Fig. 11).

7.3. Reactive melt migration and formation of gabbronorites: the case of the Peyve Seamount

The widespread occurrence of centimetric euhedral orthopyroxenes (Fig. 5) in numerous gabbronorites sampled on the southern slope of Peyve Seamount is not a common feature in oceanic settings (e.g., Grove *et al.*, 1992). In MORB-type environments, orthopyroxene is mostly documented as a late-stage magmatic phase, crystallizing interstitial and vermicular crystals around the primary magmatic phases during the closure of the magmatic system at near-solidus temperatures (e.g., Natland *et al.*, 1991; Ozawa *et al.*, 1991; Feig *et al.*, 2006; Botcharnikov *et al.*, 2008; Koepke *et al.*, 2018; Zhang *et al.*, 2020). To date, orthopyroxenes occurring as a primary magmatic phase have been reported in gabbroic rocks as a result of: *i)* interaction between percolating melts and host peridotites, leading to partial dissolution of the peridotite and to the saturation of orthopyroxene in the reactive melt (e.g., Dick and Natland, 1996; Coogan *et al.*, 2002; Suhr *et al.*, 2008; Sanfilippo *et al.*, 2016); *ii)* crystallization of depleted melts formed during shallow peridotite melting (e.g., Gillis *et al.*, 2014); *iii)* interaction between an olivine-rich gabbroic matrix and an evolved percolating melt (Bloomer *et al.*, 1991; Zellmer *et al.*, 2016; Gardner *et al.*, 2020; Zhang *et al.*, 2020).

The bulk-rock compositions of the gabbroic lithologies recovered along the Doldrums and the Vernadsky transforms define compositional trends that suggest progressive evolution of the parental melt composition from olivine gabbro to gabbro, gabbronorite and oxide gabbro (Fig. 6; Fig. 7; Fig. 8). To assess the evolution of the parental melt composition and constrain the process responsible for the saturation of primary orthopyroxene, we computed the trace element composition of the parental melts from the different lithologies recovered. The composition of melts calculated in equilibrium with clinopyroxene crystal cores (Supplementary Table S7), using the compilation of partition coefficients from Basch *et al.* (2018), are shown in Figure 12. The melts in equilibrium with the olivine gabbros and gabbros are characterized by MORB-type compositions (Fig. 12a), with LREE/MREE fractionation similar to a typical N-MORB (after Workman and Hart, 2005) and to the basalts recovered from the top of Peyve Seamount (Fig. 12a). However, upon differentiation

of the parental melt, the progressive increase in REE concentrations appears to have been accompanied by Zr-Hf enrichments and variations in the LREE/MREE and LREE/HREE ratios. The parental melts of oxide gabbros show low Zr-Hf and LREE contents Fig. 12a), whereas the parental melts of the gabbronorites are characterized by strong Zr-Hf and LREE enrichments (Fig. 12b). Since the strongest preferential enrichments in highly incompatible trace elements are found in the orthopyroxene-bearing samples, we infer that the petrological process that was responsible for the saturation in primary orthopyroxene also triggered preferential enrichments in highly incompatible trace elements.

Several processes have been proposed to explain highly incompatible trace element enrichments in mineral phases, with different implications for the evolution of the magmatic system: *i)* diffusive reequilibration at sub-solidus conditions (e.g., Coogan and O'Hara, 2015); *ii)* trapped melt crystallization (e.g., Bédard, 1994; Elthon *et al.*, 1992), and *iii)* reactive melt migration (e.g., Coogan *et al.*, 2000; Lissenberg and MacLeod, 2016; Sanfilippo *et al.*, 2020; Ferrando *et al.*, 2021a). Textural and geochemical arguments rule out the processes of sub-solidus diffusive reequilibration and trapped melt crystallization as responsible for the presence of orthopyroxene and trace element enrichments. Namely, diffusion at subsolidus temperature conditions (i.e., no interstitial melt remaining) leads to progressive reequilibration of compositions between the mineral phases (e.g., Costa *et al.*, 2020). Decreasing temperatures would lead to a diffusive flux of HREE from plagioclase into clinopyroxene and of LREE from clinopyroxene into plagioclase (e.g., Sun and Lissenberg, 2018). This process could therefore account for mineral trace element enrichments and variations in LREE/HREE ratios. However, such closed-system subsolidus diffusive reequilibration would not lead to any modification in the modal composition and bulk-rock major and trace element compositions. Alternatively, *in situ* crystallization of trapped melt could lead to strong enrichments in highly incompatible elements at mineral rims within a crystallizing gabbroic mush (e.g., Langmuir, 1989; Bédard, 1994). Closed-system melt differentiation could trigger orthopyroxene saturation and reproduce the LREE and HFSE enrichments reported in the studied samples. However, the occurrence of euhedral centimetre-size orthopyroxene in gabbronorites (Fig. 5a,b) and the strong trace element enrichments observed not only at the rims but also within clinopyroxene cores (Fig. 10a,b; Fig. 12b) militate against their crystallization from small amounts of interstitial melt as required during trapped melt crystallization (Langmuir, 1989). Rather, the documented bulk-rock enrichments in highly incompatible elements (Fig. 8) imply the addition of an external metasomatic component (e.g., Sanfilippo *et al.*, 2020). The latter corresponds to a migrating melt, which chemical disequilibrium with the crystal matrix drives dissolution-

precipitation reactions, continuously modifying the melt composition and leading to the observed early saturation of orthopyroxene and trace element enrichments.

Melts computed in equilibrium with the olivine gabbros and gabbros are characterized by MORB-type compositions (Fig. 12a), whereas the melts in equilibrium with the gabbronorites and oxide gabbros show variable enrichments in highly incompatible trace elements (Fig. 12a,b). This suggests that the inferred reactive migration process progressively modified the melt composition upon differentiation and reaction. Although interaction between mantle peridotites and MORB-type melts has been widely documented as a process driving orthopyroxene saturation in the reacted melt (e.g., Dick and Natland, 1996; Coogan *et al.*, 2002; Suhr *et al.*, 2008; Sanfilippo *et al.*, 2016; Zhang *et al.*, 2020), partial dissolution of the LREE-depleted phases forming the mantle peridotites, namely olivine, orthopyroxene and minor clinopyroxene, would further deplete the melt in the most incompatible trace elements. This is in contradiction with the enrichments in highly incompatible elements documented in the studied gabbronorites and oxide gabbros (Fig. 12), in turn suggesting that the reactive melt migration process did not involve partial dissolution of mantle peridotites. Alternatively, dissolution of plagioclase and olivine from partly crystallized gabbroic crystal mushes has been widely documented in abyssal gabbros where, when coupled to the crystallization of new phases, it causes preferential enrichments in the most incompatible trace elements in the reacted melt (e.g., Lissenberg and MacLeod, 2016; Lissenberg *et al.*, 2019; Sanfilippo et al., 2020). It is worth noting that Liang (2003) demonstrated numerically and experimentally that rapid element diffusion in the melt phase occurs concomitantly with dissolution-precipitation reactions and is able to even out the chemical gradients that form at the crystal-melt interface and thus distribute uniformly the preferential enrichments in the interstitial melt. Such melt-mush reactive processes have been widely documented in the gabbros from the Mid-Atlantic Ridge (Coogan *et al.*, 2000; Lissenberg and Dick, 2008; Brunelli *et al.*, 2020), the Southwest Indian Ridge (Boulanger *et al.*, 2020; Sanfilippo *et al.*, 2020; Zhang *et al.*, 2020, 2021, Ferrando *et al.*, 2021a, 2021b), the East Pacific Rise (Hess Deep: Lissenberg *et al.*, 2013), and several ophiolitic occurrences (e.g., Bédard and Hébert, 1996; Liu et al., 2018; Tribuzio *et al.*, 2020; Basch *et al.*, 2022). Moreover, at the Atlantis Bank OCC, Gardner *et al.* (2020) and Zhang *et al.* (2020) documented the occurrence of substantial amounts of orthopyroxene in deformed olivine gabbros. They interpreted these distinct modal compositions as resulting from reactions between an oxide-saturated melt and a primitive gabbroic crystal mush. Yet, the possibility that orthopyroxene saturation resulted from melt-rock reactions has not been explored in detail and is merely inferred.

7.3.1. Modeling reaction-driven orthopyroxene saturation

To assess whether partial dissolution of a primitive gabbroic crystal mush is able to drive orthopyroxene saturation during fractionation of evolved MORB-type melts, we performed thermodynamic modeling of reactive fractional crystallization using the *MELTS* software (Ghiorso and Sack, 1995). The composition of the basalt S45-07-173, a relatively evolved N-MORB (Mg# = 56.78; Ca# = 66.15) sampled at the Seamount Peyve (Fig. 1b), has been selected as the starting melt composition. We computed a fractional crystallization process at a constant pressure of 2 kbar and temperatures decreasing from 1160°C to 1050°C with cooling steps of 5°C. Different models have been performed, involving the assimilation of various quantities of a primitive gabbroic crystal mush (ol:plg:cpx = 10:50:40 vol%), from 0.5g/°C of cooling to 2g/°C (Supplementary Table S8). Mineral assimilation occurs through chemical dissolution, which endothermic character is taken into account into the modeled evolution of the system. Figure 13 compares the evolution of the modal composition of the solids fractionated in all models. Simple fractional crystallization leads to the formation of an oxide gabbro (plg:cpx:ox = 45:43:12 vol% at 1050°C; Fig. 13a), whereas the models involving assimilation of a primitive gabbroic mush show the early saturation of orthopyroxene upon fractionation. Notably, orthopyroxene appears as a liquidus phase at higher temperatures for higher assimilated masses (Fig. 13b-e). At assimilation rates of 0.5g/°C, orthopyroxene fractionates from 1085°C and the reactive crystallization process leads to the formation of an orthopyroxene-bearing oxide gabbro (pl:cpx:opx:ox = 45:47:4:4 vol% at 1050°C; Fig. 13b). At higher assimilation rates (2g/°C), orthopyroxene saturates at 1145°C and the reactive crystallization process leads to the formation of a gabbronorite (pl:cpx:opx:ox = 43:40:14:3 vol% at 1050°C; Fig. 13e). Interestingly, the saturation temperature of orthopyroxene in all models corresponds to the temperature at which the ratio between the assimilated mass and the crystallized mass reaches Ma/Mc = 0.7. The higher this ratio is, the stronger the influence of the assimilation process on melt evolution. The results of these thermodynamic models therefore suggest that, at high assimilation rates, the partial dissolution of a primitive gabbroic crystal mush during concomitant fractionation of an evolved MORB-type melt allows for the early saturation of orthopyroxene in the reacted melt.

7.3.2. Modeling of reaction-driven trace element enrichments

We infer that a process of reactive melt migration, during which an evolved melt partially assimilates a primitive crystal mush, is responsible for both the saturation of primary orthopyroxene and the strong highly incompatible trace element (LREE, HFSE) enrichments documented in the gabbronorites (Fig. 8b; Fig. 12b). Accordingly, we selected similar parameters to the previous *MELTS* thermodynamic models to perform trace element modeling of Assimilation-Fractional

Crystallization (AFC). Given that our aim is to reproduce mathematically the enrichments in highly incompatible elements driven by the well-constrained petrological process leading to orthopyroxene saturation, we chose to model AFC processes using the equation of De Paolo (1981), instead of more complex geochemical and thermodynamic models available in literature (e.g., Magma Chamber Simulator, see Bohrson *et al.*, 2014, 2020; Heinonen *et al.*, 2020).

The trace element composition of the basalt S45-07-173 (Yb_N = 24.8; La_N/Yb_N = 0.71) was chosen as starting melt composition, and the assimilated rock is a primitive gabbroic crystal mush, similar to the previous *MELTS* models (ol:plg:cpx = 10:50:40 vol%). We computed fractional crystallization assuming concomitant assimilation at Ma/Mc ratios ranging from 0 to 0.9. Since the AFC models do not provide thermodynamic constraints on the fractionated phases, we used the previous MELTS models to define the modal composition of the fractionated phases at a given Ma/Mc ratio. Namely, we modeled the fractionation of an oxide gabbro (plg:cpx:ox = 50:45:5 vol%) at Ma/Mc < 0.7 and the fractionation of a gabbronorite (plg:cpx:opx:ox = 50:40:8:2 vol%) at Ma/Mc > 0.7.

Figure 14 compares the composition of clinopyroxenes analyzed within the studied samples with the compositional trends of clinopyroxenes computed in equilibrium with the fractionating melt, at variable Ma/Mc ratios. The computed compositional trends clearly indicate that LREE/MREE ratios do not substantially vary during a fractional crystallization process (FC in Fig. 14), whereas strong enrichments in LREE respect to M-HREE are produced at high Ma/Mc ratios (Fig. 14). Notably, the threshold of Ma/Mc ratio observed for orthopyroxene saturation in the MELTS models is consistent with the computed trends of clinopyroxene compositions, i.e., clinopyroxenes analyzed within the gabbronorites show high LREE/MREE ratios and plot above the threshold trend of Ma/Mc = 0.7, whereas clinopyroxenes analyzed within the oxide gabbros are characterized by low values of LREE/HREE fractionation, high HREE contents and plot below the threshold of Ma/Mc = 0.7 (Fig. 14).

To better visualize the evolution of the trace element compositions within the reacted melt upon differentiation (i.e., at decreasing melt mass and temperature), we plotted the detailed trace element evolution along two AFC trends representative of the formation of oxide gabbros (plg:cpx:ox = 50:45:5 vol%) and gabbronorites (plg:cpx:opx:ox = 50:40:8:2 vol%) (Supplementary Table S8). Consistently with the compositional trends documented in Figure 14, reactive crystallization of oxide gabbros and gabbronorites, involving low (Ma/Mc = 0.3; Fig. 15a) and high (Ma/Mc = 0.8; Fig. 15b) assimilated mass, respectively, reproduce the trace element patterns of the melts computed in equilibrium with clinopyroxene cores (Fig. 15). Notably, the high LREE/MREE fractionation documented in the gabbronorites is caused by a lower increase in MREE-HREE upon progressive

differentiation (Fig. 15b). Our thermodynamic and geochemical models therefore indicate that a process of assimilation of primitive gabbroic crystal mush within an evolved MORB-type melt can be responsible for the early saturation of orthopyroxene (Fig. 13), the increase in LREE/M-HREE ratios and the high HFSE contents (Fig. 14; Fig. 15b).

7.4. Melt-rock reaction as the main process forming oceanic gabbronorites?

This study documents a well-constrained reaction-driven formation process for oceanic gabbronorites and related oxide gabbro(norite)s, the assimilated mass and the Ma/Mc ratio being the driving parameters of orthopyroxene saturation. In the context of transform walls, the process of melt/rock reaction accompanied lateral differentiation of the melts produced at the edges of the ridge segment (Fig. 11; e.g., Brunelli *et al.*, 2020). Notably, melt migration and concomitant lateral differentiation increase the chemical gradient between the percolating melt and the host rock, and therefore facilitates dissolution-precipitation reactions between a hot and primitive gabbroic crystal mush and invading melts (Fig. 16a; e.g., Liang, 2003). Diffuse percolation of the reactive melts in a hot system (Fig. 16a) is further supported by an irregular contact found between gabbronoritic and oxide gabbro portions of a studied thin section (S45-7-4B; Fig. S3a). Across this lithological contact, drastic within-sample variations in clinopyroxene core REE compositions (La_N/Sm_N = 0.118-0.490; Fig. S3b,c) point to millimetre-scale variations in assimilated mass, with Ma/Mc varying from 0 to 0.9 (Fig. S3c); the assimilated mass controls the formation of either a gabbronoritic assemblage or an oxide gabbro. This local melt hybridization implies that the chemical evolution of the melt was isolated at the scale of millimetric apophyses (Fig. 16b), each characterized by its intrinsic reactivity towards the primitive gabbroic mush, as a function of the melt composition and temperature (e.g., Liang, 2003).

It is worth noting that although melt hybridization is facilitated by the high reactivity of the melts migrating laterally at segment edges, the reactive formation of gabbronorites is not limited to transform walls. Gabbronoritic samples from IODP Hole U1473A (Atlantis Bank, Southwest Indian ridge) were interpreted as formed after reaction between a gabbroic crystal mush and an evolved percolating melt (i.e., Zhang *et al.*, 2020). These gabbronorites show La_N/Sm_N ratios in clinopyroxene similar to the compositions analysed in the gabbronorites from Peyve Seamount (Fig. 14). This indicates an elevated assimilated mass and Ma/Mc ratios (Ma/Mc = 0.8-0.9) during reactive crystallization of the gabbronorites from the Atlantis Bank, in turn suggesting that the reactive processes documented in this study occur in the core of the Atlantis Bank gabbroic section as well. At IODP Hole 1309D (Atlantis Massif, Mid-Atlantic ridge), gabbronorites have been documented in the lower part of the drillcore (depth > 620 mbsf; Suhr *et al.*, 2008; Godard *et al.*,

2009). These gabbronorites show bulk-rock major and trace element compositions as primitive as the olivine gabbros and gabbros from Hole 1309D and are often associated with olivine-rich troctolites. The latter lithology has been extensively studied in recent years and has been interpreted as the replacive product of melt-rock interaction between a percolating melt and the host mantle peridotite (e.g., Suhr *et al.*, 2008; Drouin *et al.*, 2009; Ferrando *et al.*, 2018, 2020). We here infer that the common association between gabbronorites and olivine-rich troctolites is not fortuitous. The reactive formation of olivine-rich troctolites and the related dissolution of mantle orthopyroxene drove orthopyroxene saturation within the residual melt, that subsequently led to the formation of gabbronorites instead of gabbros (Collier and Kelemen, 2010; Sanfilippo *et al.*, 2016). The formation of gabbronorites from the Atlantis Massif thus did not involve reaction with a gabbroic crystal mush, but we emphasize that it resulted from the reaction between a percolating melt and its host peridotite, thus corroborating a ubiquitous reactive origin of gabbronorites from MORB melts in oceanic environments. Conversely, at the Vema Lithospheric Section (Mid-Atlantic ridge), most gabbros show an elevated modal content in Fe-Ti oxides, and only few samples show the occurrence of orthopyroxene. Although Brunelli *et al.* (2020) interpreted the origin of these oxide gabbros to be related with melt-mush interactions, they did not report the incompatible trace element compositions of the rock-forming minerals, precluding a direct comparison with our results. Yet, considering the output of our models (Fig. 13; Fig. 14, Fig. 15), we can infer that the reactive processes forming the oxide gabbros at the Vema transverse ridge did not involve extensive assimilation (Ma/Mc < 0.7) and therefore did not allow for the saturation of orthopyroxene in the reacted melt. Therefore, we here propose that the genesis of oceanic gabbronorites by melt-rock reaction can be a ubiquitous process in the oceanic lithosphere but requires substantial amounts of assimilation to allow for early orthopyroxene saturation.

8. CONCLUSIONS

The gabbroic crust recovered along the Doldrums and Vernadsky transforms shows an evolved bulk composition, suggesting some extent of fractionation of the parental melts prior to their intrusion and exhumation at transform valley walls. The excess in Fe-Ti oxides in the gabbroic rocks can be explained by lateral differentiation of MORB melts during their migration from the segment edges towards a ridge-transform intersection, as previously reported in other gabbroic occurrences from transform valley walls worldwide. Additionally, the studied gabbroic sequence shows the common occurrence of coarse-grained euhedral orthopyroxene, which presence is not predicted during fractional crystallization of tholeiitic melts. The gabbronorites also show preferential enrichments in highly incompatible trace elements (LREE, HFSE) relative to the

neighbouring trace elements, evidenced in both bulk-rock and mineral compositions. Thermodynamic *MELTS* models and AFC calculations coherently show that reaction of an evolved MORB melt, invading and partially assimilating a primitive gabbroic crystal mush, can trigger the early saturation of primary orthopyroxene and lead to preferential enrichments in LREE and HFSE in the crystallizing phases. This study therefore documents a well-constrained case in which oceanic gabbronorites are produced by melt-rock interaction processes, the assimilated mass being the driving parameter for orthopyroxene saturation. Reactive melt migration is likely a consequence of lateral differentiation processes, themselves enhanced by the low melt production beneath ridge-segment edges and by the active tectonics in the transform domain. However, we infer that the genesis of gabbronorites by melt-rock reaction is not limited to oceanic transforms but is likely ubiquitous in the oceanic lithosphere.

ACKNOWLEDGEMENTS

We thank Barbara John for her work as editor and Matthew Loocke and Ronald B. Frost for constructive comments that helped improve the clarity of the manuscript. We would like to thank the captain, the officers, and the crew of *R/V Akademik Nikolaj Strakhov*. We also thank Andrea Risplendente for his assistance with EPMA analyses at Università degli Studi di Milano, as well as Antonio Langone for his assistance with the LA-ICP-MS analyses at the CNR-IGG, Unità di Pavia.

FUNDING

This research was supported by the Italian Programma di Rilevante Interesse Nazionale through the grant [PRIN 2017 Prot.2017KX5ZX8], by the Accordo Bilaterale CNR/RFBR 2018-2020 through the grant [CUPB36C17000250005], by the Russian Foundation for the Basic Research project no. [18-55-7806 Ital_t], and by the Russian Basic Research Program projects no. [0135-2019-0050, FMMG-2022-0003].

REFERENCES

Akizawa, N., Ohara, Y., Okino, K., Ishizuka, O., Yamashita, H., Machida, S., Sanfilippo, A., Basch, V., Snow, J. E., Sen, A., Hirauchi, K., Michibayashi, K., Harigane, Y., Fujii, M., Asanuma, H. & Hirata, T. (2021). Geochemical characteristics of back-arc basin lower crust and

upper mantle at final spreading stage of Shikoku Basin: an example of Mado Megamullion. *Progress in Earth and Planetary Science*, **8**, 65, doi: 10.1186/s40645-021-00454-3.

Auzende, J.-M., Bideau, D., Bonatti, E., Cannat, M., Honnorez, J., Lagabrielle, Y., Malavieille, J., Mamaloukas-Frangoulis, V. & Mevel, C. (1989). Direct observation of a section through slow-spreading oceanic crust. *Nature*, **337**, 726-729, doi: 10.1038/337726a0.

Auzende, J. M., Cannat, M., Gente, P., Henriet, J. P., Juteau, T., Karson, J., Lagabrielle, Y., Mével, C. & Tivey, M. (1994) Observation of sections of oceanic crust and mantle cropping out on the southern wall of Kane FZ (N. Atlantic). *Terra Nova*, **6**, 143-148.

Bai, H. & Montési, L. G. J. (2015). Slip-rate-dependent melt extraction at oceanic transform faults. *Geochemistry, Geophysics, Geosystems*, **16**, 401-419, doi: 10.1002/2014GC005579.

Basch, V., Rampone, E., Crispini, L., Ferrando, C., Ildefonse, B. & Godard, M. (2018). From mantle peridotites to hybrid troctolites: textural and chemical evolution during melt–rock interaction history (Mt. Maggiore, Corsica, France). *Lithos*, **323**, 4–23, doi: 10.1016/j.lithos.2018.02.025.

Basch, V., Rampone, E., Borghini, G., Ferrando, C. & Zanetti, A. (2019a). Origin of pyroxenites in the oceanic mantle and their implications on the reactive percolation of depleted melts. *Contributions to Mineralogy and Petrology*, **174**, 97, doi: 10.1007/s00410-019-1640-0.

Basch, V., Rampone, E., Crispini, L., Ferrando, C., Ildefonse, B. & Godard, M. (2019b). Multi-stage reactive formation of troctolites in slow-spreading oceanic lithosphere (Erro-Tobbio, Italy): a combined field and petrogeochemical study. *Journal of Petrology*, **60**, 873-906, doi: 10.1093/petrology/egz019.

Basch, V., Sanfilippo, A., Sani, C., Ohara, Y., Snow, J., Ishizuka, O., Harigane, Y., Michibayashi, K., Sen, A., Akizawa, N., Okino, K., Fujii, M. & Yamashita, H. (2020). Crustal accretion in a slow-spreading back-arc basin: Insights from the Mado Megamullion oceanic core complex in the Shikoku Basin. *Geochemistry, Geophysics, Geosystems*, **21**, e2020GC009199, doi: 10.1029/2020gc009199.

Basch, V., Sanfilippo, A., Vigliotti, L., Langone, A., Rasul, N., Khorsheed, M., AlNomani, S., AlQutub, A. & Ligi, M. (2022). Crustal contamination and hybridization of an embryonic oceanic crust during the Red Sea rifting (Tihama Asir igneous complex, Saudi Arabia). *Journal of Petrology*, in press, doi: 10.1093/petrology/egac005

Bédard, J. H. (1994). A procedure for calculating the equilibrium distribution of trace elements among the minerals of cumulate rocks, and the concentration of trace elements in coexisting liquids. *Chemical Geology*, **118**, 143-153, doi: 10.1016/0009-2541(94)90173-2.

Bédard, J. H., & Hébert, R. (1996). The lower crust of the Bay of Islands ophiolite, Canada: Petrology, mineralogy and the importance of syntexis in magmatic differentiation. *Journal of Geophysical Research*, **101**, 25105-25124.

Behn, M. D. & Ito, G. (2008). Magmatic and tectonic extension at mid-ocean ridges: 1. Controls on fault characteristics. *Geochemistry, Geophysics, Geosystems*, **9**, Q08O10, doi: 10.1029/2008GC001965.

Bennett, E. N., Jenner, F. E., Millet, M.-A., Cashman, K. V. & Lissenberg, C. J. (2019). Deep roots for mid-ocean-ridge volcanoes revealed by plagioclase-hosted melt inclusions. *Nature*, **572**, 235-239, doi: 10.1038/s41586-019-1448-0

Bickert, M., Cannat, M., Tommasi, A., Jammes, S. & Lavier, L. (2021). Strain localization in the root of detachment faults at a melt-starved mid-ocean ridge: a microstructural study of abyssal peridotites from the Southwest Indian Ridge. *Geochemistry, Geophysics, Geosystems*, **22**, e2020GC009434., doi: 10.1029/2020GC009434.

Blackman, D. K., Karson, J. A., Kelley, D. S., Cann, J. R., Früh-Green, G. L., Gee, J., S., Hurst, S. D., John, B. E., Morgan, J., Nooner, S. L., Ross, D. K., Shroeder, T. J. & Williams, E. A. (2002). Geology of the Atlantis Massif (Mid-Atlantic Ridge, 30° N): Implications for the evolution of an ultramafic oceanic core complex. *Marine Geophysical Researches*, **23**, 443-469, doi: 10.1023/B:MARI.0000018232.14085.75.

Blackman, D. K., Ildefonse, B., John, B. E., Ohara, Y., Miller, D. J., Abe, N., Abratis, M., Andal, E. S., Andreani, M., Awaji, S., Beard, J. S., Brunelli, D., Charney, A. B., Christie, D. M., Collins, J., Delacour, A. G., Delius, H., Drouin, M., Einaudi, F., Escartìn, J., Frost, B. R., Früh-Green, G. L., Fryer, P. B., Gee, J. S., Godard, M., Grimes, C. B., Halfpenny, A., Hansen, H. E., Harris, A. C., Tamura, A., Hayman, N. W., Hellebrand, E., Hirose, T., Hirth, J. G., Ishimaru, S., Johnson, K. T. M., Karner, G. D., Linek, M., MacLeod, C. J., Maeda, J., Mason, O. U., McCaig, A. M., Michibayashi, K., Morris, A., Nakagawa, T., Nozaka, T., Rosner, M., Searle, R. C., Suhr, G., Tominaga, M., von der Handt, A., Yamasaki, T. & Zhao, X. (2011). Drilling constraints on lithospheric accretion and evolution at Atlantis Massif, Mid-Atlantic Ridge 30°N. *Journal of Geophysical Research*, **116**, B07103, doi: 10.1029/2010JB007931.

Bloomer, S. H., Meyer, P. S., Dick, H. J. B., Ozawa, K. & Natland, J. H. (1991). Textural and mineralogic variations in gabbroic rocks from Hole 735B. In: Von Herzen, R.P., Robinson, P.T., et al. (Eds.), *Proceedings ODP, Scientific Results*. Ocean Drilling Program, College Station, TX, **118**, 21-39.

Bonatti, E. (1978). Vertical tectonism in oceanic fracture zones. *Earth and Planetary Science Letters*, **37**, 369–379.

Bonatti, E., Ligi, M., Gasperini, L., Peyve, A., Raznitsin, Y. & Chen, Y. J. (1994). Transform migration and vertical tectonics at the Romanche fracture zone, Equatorial Atlantic. *Journal of Geophysical Research*, **99**, 21779-21802.

Bonatti, E., Ligi, M., Borsetti, A. M., Gasperini, L., Negri, A. & Sartori, R. (1996a). Lower Cretaceous deposits trapped near the Mid-Atlantic Ridge and the opening of the equatorial Atlantic. *Nature*, **380**, 518–520.

Bonatti, E., Ligi, M., Carrara, G. et al. (1996b). Diffuse impact of the Mid Atlantic Ridge with the Romanche transform: an Ultracold Ridge/Transform Intersection. *Journal of Geophysical Research*, **101**, 8043-8054.

Bonatti, E., Brunelli, D., Fabretti, P., Ligi, M., Asunta Portaro, R. & Seyler, M. (2001). Steady-state creation of crust-free lithosphere at cold spots in mid-ocean ridges. *Geology*, **29**, 979-982.

Bonatti, E., Ligi, M., Brunelli, D., Cipriani, A., Fabretti, P., Ferrante, V., Gasperini, L. & Ottolini, L. (2003). Mantle thermal pulses below the Mid-Atlantic Ridge and temporal variations in the formation of oceanic lithosphere. *Nature*, **423**, 499–505, doi: 10.1038/nature01594.

Bonatti E., Brunelli D., Buck W. R., Cipriani, A., Fabretti, P., Ferrante, V., Gasperini, L. & Ligi, M. (2005). Flexural uplift of a lithospheric slab near the Vema transform (Central Atlantic): Timing and mechanism. *Earth and Planetary Science Letters*, **240**, 642-655.

Bohrson, W. A., Spera, F. J., Ghiorso, M. S., Brown, G. A., Creamer, J. B. & Mayfield, A. (2014). Thermodynamic model for energy-constrained open system evolution of crustal magma bodies undergoing simultaneous recharge, assimilation and crystallization: the magma chamber simulator. *Journal of Petrology*, **55**, 1685–1717, doi: 10.1093/petrology/egu036.

Bohrson, W. A., Spera, F. J., Heinonen, J. S., Brown, G. A., Scruggs, M. A., Adams, J. V., Takach, M. K., Zeff, G. & Suikkanen, E. (2020). Diagnosing open-system magmatic processes using the Magma Chamber Simulator (MCS): part I-major elements and phase equilibria. *Contributions to Mineralogy and Petrology*, **175**, 104, doi: 10.1007/s00410-020-01722-z.

Boschi, C., Früh-Green, G. L., Delacour, A., Karson, J. A. & Kelley, D. S. (2006). Mass transfer and fluid flow during detachment faulting and development of an oceanic core complex, Atlantis Massif (MAR 30°N). *Geochemistry, Geophysics, Geosystems*, **7**, Q01004, doi: 10.1029/2005GC001074.

Botcharnikov, R. E., Almeev, R., Koepke, J. & Holtz, F. (2008). Phase relations and liquid lines of descent in hydrous ferrobasalt - Implications for the Skaergaard intrusion and Columbia River flood basalts. *Journal of Petrology*, **49**, 1687–1727, doi: 10.1093/petrology/egn043.

Boulanger, M., France, L., Deans, J., Ferrando, C., Lissenberg, C. J. & von der Handt, A. (2020). Magma reservoir formation and evolution at a slow-spreading center (Atlantis Bank, Southwest Indian Ridge). *Frontiers in Earth Sciences*, **8**, 554598, doi:10.3389/feart.2020.554598.

Bown, J. W. & White, R. S. (1994). Variation with spreading rate of oceanic crustal thickness and geochemistry. *Earth and Planetary Science Letters*, **121**, 435-449, doi: 10.1016/0012-821X(94)90082-5.

Brunelli, D., Sanfilippo, A., Bonatti, E, Skolotnev, S., Escartin, J., Ligi, M., Ballabio, G. & Cipriani, A. (2020). Origin of oceanic ferrodiorites by injection of nelsonitic melts in gabbros at the Vema Lithospheric Section, Mid-Atlantic Ridge. *Lithos*, **368-369**, 105589, doi: 10.1016/j.lithos.2020.105589.

Buck, W. R., Lavier, L. L. & Poliakov, A. N. B. (2005). Modes of faulting at mid-ocean ridges. *Nature*, **434**, 719-723, doi: 10.1038/nature03358.

Cande, S. C., LaBreque, J. L. & Haxby, W. F. (1988). Plate kinematics of the south Atlantic, chron C34 to the present. *Journal of Geophysical Research*, **93**, 13479-13492.

Cann, J. R., Blackman, D. K., Smith, D. K., McAllister, E., Janssen, B., Mello, S., & Pascoe, A. R., (1997). Corrugated slip surfaces formed at ridge-transform intersections on the Mid-Atlantic Ridge. *Nature*, **385**, 329-332, doi: 10.1038/385329a0.

Cannat, M., Mamaloukas-Frangoulis, V., Auzende, J. M., Bideau, D., Bonatti, E., Honnorez, J., Lagabrielle, Y., Malavieille, J. & Mevel, C. (1991). A geological cross-section of the Vema fracture zone transverse ridge, Atlantic Ocean. *Journal of Geodynamics*, **13**, 97-117, doi: 10.1016/0264-3707(91)90034-C.

Cannat, M., Sauter, D., Mendel, V., Ruellan, E., Okino, K., Escartin, J., Combier, V. & Baala, M. (2006). Modes of seafloor generation at a melt-poor ultraslow-spreading ridge. *Geology*, **34**, 605-608, doi: 10.1130/G22486.1.

Cannat, M., Sauter, D., Lavier, L., Bickert, M., Momoh, E. & Leroy, S. (2019). On spreading modes and magma supply at slow and ultraslow mid-ocean ridges. *Earth and Planetary Science Letters*, **519**, 223-233, doi: 10.1016/j.epsl.2019.05.012.

Carbotte, S. & Scheirer, D. S. (2004). Variability of ocean crustal structure created along the global Mid-Ocean Ridge. In: Davis, E. E. & Elderfield, H. (eds.) *Hydrogeology of the oceanic lithosphere*. Cambridge University Press, Cambridge, pp 59–107

Chen, Y. J. (1992). Oceanic crustal thickness versus spreading rate. *Geophysical Research Letters*, **19**, 753-756, doi: 10.1029/92GL00161.

Cipriani, A., Bonatti, E., Brunelli, D. & Ligi, M. (2009). 26 million years of mantle upwelling below a segment of the Mid Atlantic Ridge: The Vema Lithospheric Section revisited. *Earth ad Planetary Science Letters*, **285**, 87-95, doi: 10.1016/j.epsl.2009.05.046.

Collier, M. L. & Kelemen, P. B. (2010). The case for reactive crystallization at mid-ocean ridges. *Journal of Petrology*, **51**, 1913-1940, doi: 10.1093/petrology/egq043.

Coogan, L. A., Saunders, A. D., Kempton, P. D. & Norry, M. J. (2000). Evidence from oceanic gabbros for porous melt migration within a crystal mush beneath the Mid-Atlantic Ridge. *Geochemistry, Geophysics, Geosystems*, **1**, 2000GC000072, doi: 10.1029/2000GC000072.

Coogan, L. A., Gillis, K. M., MacLeod, C. J., Thompson, G. M. & Hékinian, R. (2002). Petrology and geochemistry of the lower ocean crust formed at the East Pacific Rise and exposed at Hess Deep: A synthesis and new results. *Geochemistry, Geophysics, Geosystems*, **3**, 8604, doi: 10.1029/2001GC000230.

Coogan, L. A & O'Hara, M. J. (2015). MORB differentiation: In situ crystallization in replenished-tapped magma chambers. *Geochimica et Cosmochimica Acta*, **158**, 147-161, doi: 10.1016/j.gca.2015.03.010.

Costa, F., Shea, T. & Ubide, T. (2020). Diffusion chronometry and the timescales of magmatic processes. *Nature Reviews*, **1**, 201-214, doi: 10.1038/s43017-020-0038-x.

DePaolo, D. J. (1981). Trace element and isotopic effects of combined wall-rock assimilation and fractional crystallization. *Earth and Planetary Science Letters*, **53**, 189–202, doi: 10.1016/0012-821x(81)90153-9.

Dick, H. J. B. & Natland, J. H. (1996). Late-stage melt evolution and transport in the shallow mantle beneath the East Pacific Rise. In: Mével C., Gillis K. M., Allan J. F., Meyer P. S. (eds.)

Proceedings of the Ocean Drilling Program, Scientific Results, **147**, 103-134, doi: 10.2973/odp.proc.sr.147.007.

Dick, H. J. B., Natland, J. H., Alt, J. C., Bach, W., Bideau, D., Gee, J. S., Haggas, S., Hertogen, J. G. H., Hirth, G., Holm, P. M., Ildefonse, B., Iturrino, G. J., John, B. E., Kelley, D. S., Kikawa, E., Kingdon, A., LeRoux, P. J., Maeda, J., Meyer, P. S., Miller, D. J., Naslund, H. R., Niu, Y. -L., Robinson, P. T., Snow, J., Stephen, R. A., Trimby, P. W., Worm, H. -U. & Yoshinobu, A. (2000). A long in situ section of the lower ocean crust: results of ODP Leg 176 drilling at the Southwest Indian Ridge. *Earth and Planetary Science Letters*, **179**, 31–51, doi: 10.1016/s0012-821x(00)00102-3.

Dick, H. J. B., Ozawa, K., Meyer, P. S., Niu, Y., Robinson, P. T., Constantin, M., Hebert, R., Maeda, J., Natland, J. H., Hirth, J. G. & Mackie, S. M. (2002). Primary silicate mineral chemistry of a 1.5-km section of very slow spreading lower ocean crust: ODP hole 735B, southwest Indian ridge. In: Natland, J. H., Dick, H. J. B., Miller, D. J. and Von Herzen, R. P. (eds) *Proceedings of the Ocean Drilling Program, Scientific Results*, Vol. **176**. College Station, TX: Ocean Drilling Program, pp. 1–61.

Dick, H. J. B., Natland, J. H. & Ildefonse, B. (2006). Past and future impact of deep drilling in the oceanic crust and mantle. *Oceanography*, **19**, 72-80.

Dick, H. J. B., Tivey, M. A. & Tucholke, B. E. (2008). Plutonic foundation of a slow-spreading ridge segment: Oceanic core complex at Kane Megamullion, 23°30’N, 45°20’W. *Geochemistry, Geophysics, Geosystems*, **9**, Q05014, doi: 10.1029/2007GC001645.

Dick, H. J. B, Lissenberg, C. J. & Warren, J. M. (2010). Mantle melting melt transport, and delivery beneath a slow-spreading ridge: the paleo-MAR from 23°15′N to 23°45′N. *Journal of Petrology*, **51**, 425–467, doi: 10.1093/petrology/egp088.

Dick, H. J. B., Kvassnes, A. J. S., Robinson, P. T., MacLeod, C. J. & Kinoshita, H. (2019). The Atlantis Bank Gabbro Massif, Southwest Indian Ridge. *Progress in Earth and Planetary Science*, **6**, 64, doi: 10.1186/s40645-019-0307-9.

Dijkstra, A. H., Barth, M. G., Drury, M. R., Mason, P. R. D. & Vissers, R. L. M. (2003). Diffuse porous melt flow and melt-rock reaction in the mantle lithosphere at a slow-spreading ridge: a structural petrology and LA-ICP-MS study of the Othris peridotite massif (Greece). *Geochemistry, Geophysics, Geosystems*, **4**, 8613, doi: 10.1029/2001GC000278.

Drouin, M., Godard, M., Ildefonse, B., Bruguier, O. & Garrido, C. (2009). Geochemical and petrographic evidence for magmatic impregnation in the oceanic lithosphere at Atlantis Massif, Mid-Atlantic Ridge (IODP Hole U1309D, 30°N). *Chemical Geology*, **264**, 71–88, doi: 10.1016/j.chemgeo.2009.02.013.

Elthon, D., Stewart, M. & Ross, K. D. (1992). Compositional trends of minerals in oceanic cumulates. *Journal of Geophysical Research*, **97**, 5189-5199, doi: 10.1029/92JB01187.

Feig, S., Koepke, J. & Snow, J. (2006). Effect of water on tholeiitic basalt phase equilibria: an experimental study under oxidizing conditions. *Contributions to Mineralogy and Petrology*, **152**, 611–638, doi: 10.1007/s00410-006-0123-2.

Ferrando, C., Godard, M., Ildefonse, B. & Rampone, E. (2018). Melt transport and mantle assimilation at Atlantis Massif (IODP Site U1309): constraints from geochemical modelling. *Lithos*, **323**, 24–43, doi: 10.1016/j.lithos.2018.01.012.

Ferrando, C., France, L., Basch, V., Sanfilippo, A., Tribuzio, R. & Boulanger, M. (2021a). Grain size variations record segregation of residual melts in slow-spreading oceanic crust (Atlantis Bank, 57°E Southwest Indian Ridge). *Journal of Geophysical Research: Solid Earth*, **126**, e2020JB020997, doi: 10.1029/2020JB020997.

Ferrando, C., Basch, V., Ildefonse, B., Deans, J., Sanfilippo, A., Barou, F. & France, L. (2021b). Role of compaction in melt extraction and accumulation at a slow spreading center: Microstructures of olivine gabbros from the Atlantis Bank (IODP Hole U1473A, SWIR). *Tectonophysics*, **815**, 229001, doi: 10.1016/j.tecto.2021.229001.

Fox, P. J. & Gallo D. G. (1984). A tectonic model for ridge-transform-ridge plate boundaries: Implications for the structure of oceanic lithosphere. *Tectonophysics*, **104**, 205-242.

Gardner, R. L., Piazolo, S., Daczko, N. R. & Trimby, P. (2020). Microstructures reveal multistage melt present strain localisation in mid-ocean gabbros. *Lithos*, **366-367**, 105572, doi: 10.1016/j.lithos.2020.105572.

Gillis, K. M., Snow, J. E., et al. (2014). Primitive layered gabbros from fast-spreading lower oceanic crust. *Nature*, **505**, 204-211, doi: 10.1038/nature12778.

Godard, M., Awaji, S., Hansen, H., Hellebrand, E., Brunelli, D., Johnson, K., et al. (2009). Geochemistry of a long in-situ section of intrusive slow-spread oceanic lithosphere: Results from IODP Site U1309 (Atlantis Massif, 30°N Mid-Atlantic-Ridge). *Earth and Planetary Science Letters*, **279**, 110–122, doi: 10.1016/j.epsl.2008.12.034.

Grove, T. L., Kinzler, R. J. & Bryan, W. B. (1992). Fractionation of Mid-Ocean Ridge Basalt (MORB). In: Phipps Morgan, J., Blackman, D. K. & Sinton, J. M. (Eds.) Mantle Flow and melt generation at mid-ocean ridges, *Geophysical Monograph Series*, **71**, 281-310, doi: 10.1029/GM071p0281.

Ghiorso, M. S. & Sack, O. (1995). Chemical mass transfer in magmatic processes. IV. A revised and internally consistent thermodynamic model for the interpolation and extrapolation of liquid-solid equilibria in magmatic systems at elevated temperatures and pressures. *Contributions to Mineralogy and Petrology*, **119**, 197–212, doi:10.1007/BF00307281.

Heinonen, J. S., Bohrson, W. A., Spera, F. J., Brown, G. A., Scruggs, M. & Adams, J. (2020). Diagnosing open-system magmatic processes using the Magma Chamber Simulator (MCS): part II—trace elements and isotopes. *Contributions to Mineralogy and Petrology*, **175**, 105, doi: 10.1007/s00410-020-01718-9

Hekinian, R., Juteau, T., Gràcia, E. Sichler, B., Sichel, S., Udintsev, G., Apprioual, R. & Ligi, M. (2000). Submersible observations of Equatorial Atlantic mantle: the St. Paul Fracture Zone region. *Marine Geophysical Researches*, **21**, 529, doi: 10.1023/A:1004819701870.

Hooft, E. E. E., Detrick, R. S., Toomey, D. R., Collins, J. A. & Lin, J. (2000). Crustal thickness and structure along three contrasting spreading segments of the Mid-Atlantic Ridge, 33.5°–35°N, *Journal of Geophysical. Research*, **105**, 8205-8226, doi:10.1029/1999JB900442.

Karson, J. A., Früh-Green, G. L., Kelley, D. S., Williams, E. A., Yoerger, D. R. & Jakuba, M. (2006). Detachment shear zone of the Atlantis Massif core complex, Mid-Atlantic Ridge, 30°N. *Geochemistry, Geophysics, Geosystems*, **7**, Q06016, doi: 10.1029/2005GC001109.

Klein, E. M. & Langmuir, C. H. (1987). Global correlations of ocean ridge basalt chemistry with axial depth and crustal thickness. *Journal of Geophysical Research*, **92**, 8089-8115.

Koepke, J., Botcharnikov, R. E. & Natland, J. H. (2018). Crystallization of late-stage MORB under varying water activities and redox conditions: Implications for the formation of highly evolved lavas and oxide gabbro in the ocean crust. *Lithos*, **323**, 58-77, doi: 10.1016/j.lithos.2018.10.001.

Langmuir, C.H. (1989). Geochemical consequences of in situ crystallization. *Nature* **340**, 199-205, doi: 10.1038/340199a0.

Langmuir, C. H. & Forsyth, D. W. (2007). Mantle melting beneath mid-ocean ridges. *Oceanography* **20**, 78–89.

Leake, B. E., Woolley, A. R., Arps, C. E. S., Birch, W. D., Gilbert, M. C., Grice, J. D., et al. (1997). Nomenclature of amphiboles: Report of the subcommittee on amphiboles of the International Mineralogical Association Commission on New Minerals and Mineral Names. *The Canadian Mineralogist*, **35**, 219–246.

Liang, Y. (2003). Kinetics of crystal–melt reaction in partially molten silicates: 1. Grain scale processes. *Geochemistry, Geophysics, Geosystems*, **4**, 1045, doi:10.1029/2002GC000375.

Ligi, M., Bonatti, E., Gasperini, L. & Poliakov, A. N. B. (2002). Oceanic broad multifault transform plate boundaries. *Geology*, **30**, 11-14.

Ligi, M., Bonatti, E., Cipriani, A. & Ottolini, L. (2005). Water-rich basalts at mid-ocean-ridge cold spots. *Nature*, **434**: 66-69.

Lissenberg, C. J. & Dick, H. J. B. (2008). Melt–rock reaction in the lower oceanic crust and its implications for the genesis of mid-ocean ridge basalt. *Earth and Planetary Science Letters*, **271**, 311–325, doi: 10.1016/j.epsl.2008.04.023.

Lissenberg, C. J., MacLeod, C. J., Howard, K. A. & Godard, M. (2013). Pervasive reactive melt migration through fast-spreading lower oceanic crust (Hess Deep, equatorial Pacific Ocean). *Earth and Planetary Science Letters*, **361**, 436-447, doi: 10.1016/j.epsl.2012.11.012.

Lissenberg, C. J. & MacLeod, C. J. (2016). A reactive porous flow control on mid-ocean ridge magmatic evolution. *Journal of Petrology*, **57**, 2195-2220, doi: 10.1093/petrology/egw074.

Lissenberg, C. J., MacLeod, C. J. & Bennett, E. N. (2019). Consequences of a crystal mush-dominated magma plumbing system: a mid-ocean ridge perspective. *Philosophical Transactions of the Royal Society A*, **377**, 20180014, doi: 10.1098/rsta.2018.0014.

Liu, T., Wu, F.-Y., Liu, C.-Z., Tribuzio, R., Ji, W.-B., Zhang, C., Xu, Y. & Zhang, W.-Q. (2018). Variably evolved gabbroic intrusions within the Xigaze ophiolite (Tibet): new insights into the origin of ophiolite diversity. *Contributions to Mineralogy and Petrology*, **173**, 91, doi: 10.1007/s00410-018-1518-6.

Luo, Y., Lin, J., Zhang, F. & Wei, M. (2021). Spreading rate dependance of morphological characteristics in global oceanic transform faults. *Acta Oceanologica Sinica*, **40**, 39-64, doi: 10.1007/s13131-021-1722-5.

MacLeod, C. J., Dick, H. J. B., Blum, P. et al. (2017). Expedition 360 summary. In: MacLeod, C. J., Dick, H. J. B., Blum, P. and the Expedition 360 Scientists (Eds.), Southwest Indian Ridge lower

crust and Moho. *Proceedings of the International Ocean Discovery Program*, Vol. **360**: 1-267, doi: 10.14379/iodp.proc.360.103.2017.

Maia, M., Sichel, S., Briais, A. et al. (2016). Extreme mantle uplift and exhumation along a transpressive transform fault. *Nature Geoscience*, **9**, 619-624, doi: 10.1038/NGEO2759.

Maia, M. (2019). Chapter 3 - Topographic and Morphologic Evidences of Deformation at Oceanic Transform Faults: Far-Field and Local-Field Stresses. In: Duarte, J. C. (eds) *Transform Plate Boundaries and Fracture Zones*, 61-87, doi: 10.1016/B978-0-12-812064-4.00003-7.

Mével, C., Cannat, M., Gente, P., Marion, E., Auzende, J. M. & Karson, J. A. (1991) Emplacement of deep crustal and mantle rocks on the west median valley wall of the MARK area (MAR, 23°N). *Tectonophysics*, **190**, 31-53, doi: 10.1016/0040-1951(91)90353-T.

Miller, D. J., Abratis, M., Christie, D., Drouin, M., Godard, M., Ildefonse, B., Maeda, J., Weinsteiger, A., Yamasaki, T., Suzuki, Y., Niino, A., Sato, Y. & Takeda, F. (2009). Data report: microprobe analyses of primary mineral phases from site U1309, Atlantis Massif, IODP Expedition 304/305. In: Blackman, D. K., Ildefonse, B., John, B. E., Ohara, Y., Miller, D. J., MacLeod, C. J. & the Expedition 304/305 Scientists (eds.) *Proceedings of the International Ocean Drilling Program*, **304/305**. College Station, TX: Integrated Ocean Drilling Program, p. 4.

Natland, J. H., Meyer, P. S., Dick, H. J. B. & Bloomer, S. H. (1991). Magmatic oxides and sulfides in gabbroic rocks from ODP Hole 735B and the later development of the liquid line of descent. In: Von Herzen, R.P., Robinson, P.T., et al. (Eds.), *Proceedings ODP, Scientific Results. Ocean Drilling Program, College Station, TX*, **118**, 75–111, doi: 10.2973/odp.proc.sr.118.163.1991.

Niu, Y. & Hékinian, R. (1997). Spreading-rate dependence of the extent of mantle melting beneath ocean ridges. *Nature*, **385**, 326–329

Niu, Y. (1997). Mantle melting and melt extraction processes beneath ocean ridges: evidence from abyssal peridotites. *Journal of Petrology*, **38**, 1047–1074.

Niu, Y. (2021). Lithosphere thickness controls the extent of mantle melting, depth of melt extraction and basalt compositions in all tectonic settings on Earth – A review and new perspectives. *Earth-Science Reviews*, **217**: 103614, doi: 10.1016/j.earscirev.2021.103614.

Olive, J.-A. & Dublanchet, P. (2020). Controls on the magmatic fraction of extension at mid-ocean ridges. *Earth and Planetary Science Letters*, **549**, 116541, doi: 10.1016/j.epsl.2020.116541.

Ozawa, K., Meyer, P. S. & Bloomer, S. H. (1991). Mineralogy and textures of iron-titanium-oxide gabbros from hole 735B. In: Von Herzen, R.P., Robinson, P.T., et al. (Eds.), *Proceedings ODP, Scientific Results. Ocean Drilling Program, College Station, TX*, **118**, 41–73, doi: 10.2973/odp.proc.sr.118.125.1991.

Parmentier, E. M. & Phipps Morgan, J. (1990). Spreading rate dependence of three-dimensional structure in oceanic spreading centres. *Nature*, **348**, 325-328.

Pushcharovsky, Yu. M., Raznitsin, Yu. N., Mazarovich, A. O. et al. (1991). Structure of the Doldrums fracture zone Central Atlantic. *M. Nauka*, 224 pp. (in Russian).

Pushcharovsky, Yu. M., Raznitsin, Yu. N., Mazarovich, A.O., Skolotnev, S. G., Kepezinskas, P. K., Tyrko, N. N., Peyve, A. A. & Dmitriev, D. A. (1992). Fracture zones Arkhangelsky, Doldrums and Vernadsky in the Central Atlantic: structure and rocks composition. *Geotectonika*, **6**, 63-79 (in Russian).

Rampone, E., Borghini, G. & Basch, V. (2020). Melt migration and melt–rock reaction in the Alpine-Apennine peridotites: insights on mantle dynamics in extending lithosphere. *Geoscience Frontiers*, **11**, 151-166, doi: 10.1016/j.gsf.2018.11.001.

Sandwell, D. T. & Smith, W. H. F. (1997). Marine gravity anomaly from Geasat and ERS-1 satellite altimetry: *Journal of Geophysical Research*, **102**, 10039-10054.

Sanfilippo, A., Tribuzio, R. & Tiepolo, M. (2014). Mantle-crust interactions in the oceanic lithosphere: Constraints from minor and trace elements in olivine. *Geochimica et Cosmochimica Acta*, **141**, 423-439, doi: 10.1016/j.gca.2014.06.012.

Sanfilippo, A., Dick, H. J. B., Ohara, Y. & Tiepolo, M. (2016). New insights on the origin of troctolites from the breakaway area of the Godzilla Megamullion (Parece Vela back-arc basin): The role of melt-mantle interaction on the composition of the lower crust. *Island Arc*, **25**, 220-234, doi: 10.1111/iar.12137.

Sanfilippo, A., Dick, H. J. B., Marschall, H. R., Lissenberg, C. J. & Urann, B. (2019). Emplacement and high-temperature evolution of gabbros of the 16.5°N oceanic core complexes (Mid-Atlantic Ridge): Insights into the compositional variability of the lower oceanic crust. *Geochemistry, Geophysics, Geosystems*, **20**, 46-66, doi: 10.1029/2018GC007512.

Sanfilippo, A., MacLeod, C.J., Tribuzio, R., Lissenberg, C.J. & Zanetti, A. (2020). Early-stage melt-rock reaction in a cooling crystal mush beneath a slow-spreading mid-ocean ridge (IODP

Hole U1473A, Atlantis Bank, Southwest Indian Ridge). *Frontiers in Earth Science*, **8**, 579138, doi: 10.3389/feart.2020.579138.

Sani, C., Sanfilippo, A., Ferrando, C., Peyve, A. A., Skolotnev, S. G., Muccini, F., Zanetti, A., Basch, V., Palmiotto, C., Bonatti, E. & Ligi, M. (2020). Ultra-depleted melt refertilization of mantle peridotites in a large intra-transform domain (Doldrums Fracture Zone; 7-8°N, Mid Atlantic Ridge). *Lithos*, **374-375**, 105698, doi: 10.1016/j.lithos.2020.105698.

Schilling, J. G., Ruppel, C., Davis, A. N., McCully, B., Tighe, S. A., Kingsley, R. H. & Lin, J. (1995). Thermal structure of the mantle beneath the equatorial mid-Atlantic ridge - Inferences from the spatial variation of dredged basalt glass compositions. *Journal of Geophysical Research*, **100**, 10057–10076.

Searle, R. C., Thomas, M. V. & Jones, E. J. W. (1994). Morphology and tectonics of the Romanche Transform and its environs. *Marine Geophysical Researches*, **16**, 427-453.

Skolotnev, S. G., Sanfilippo, A., Peyve, A. A., Muccini, F., Sokolov, S. Y., Sani, C., Dobroliubova, K. O., Ferrando, C., Chamov, N. P., Palmiotto, C., Pertsev, A. N., Bonatti, E., Cuffaro, M., Gryaznova, A. C., Sholukhov, K. N., Bich, A. S. & Ligi, M. (2020). Large-scale structure of the Doldrums multi-fault transform system (7-8°N Equatorial Atlantic): preliminary results from the 45th expedition of the R/V A.N. Strakhov. *Ofioliti*, **45**: 25-41.

Suhr, G., Hellebrand, E., Johnson, K. & Brunelli, D. (2008). Stacked gabbro units and intervening mantle: a detailed look at a section of IODP Leg 305, Hole U1309D. *Geochemistry, Geophysics, Geosystems*, **9**, doi: 10.1029/2008GC002012.

Sun, S. -S. & McDonough, W. F. (1989). Chemical and isotopic systematics of oceanic basalts: implications for mantle composition and processes. In: Saunders AD, Norry MJ (eds) Magmatism in the ocean basins, Vol **42**. *Geological Society, London*, pp 313–345 (Special Publications).

Takeuchi, C. S., Sclater, J. G., Grindlay, N. R., Madsen, J. A. & Rommevaux-Jestin, C. (2010). Segment-scale and intrasegment lithospheric thickness and melt variations near the Andrew Bain megatransform fault and Marion hot spot: Southwest Indian Ridge, 25.5°E-35°E. *Geochemistry, Geophysics, Geosystems*, **11**, Q07012, doi: 10.1029/2010GC003054.

Tribuzio, R., Manatschal, G., Renna, M. R., Ottolini, L. & Zanetti, A. (2020). Tectono-magmatic interplay and related metasomatism in gabbros of the Chenaillet ophiolite (Western Alps). *Journal of Petrology*, **60**, 2483-2508, doi: 10.1093/petrology/egaa015.

Tucholke, B. E., Behn, M. D., Buck, W. R. & Lin, J. (2008). Role of melt supply in oceanic detachment faulting and formation of megamullions. *Geology*, **36**, 455-458, doi: 10.1130/G24639A.1

Warren, J. M. & Shimizu, N. (2010). Cryptic variations in abyssal peridotite compositions: evidence for shallow-level melt infiltration in the oceanic lithosphere. *Journal of Petrology*, **51**: 395–423, doi: 10.1093/petro logy/egp096.

White, W. M., Klein, E. M. (2014). Composition of the Oceanic crust. In: Turekian, K. & Holland, H. (eds.) *Treatise on Geochemistry 2nd Edition*, **4**, 457-496, doi: 10.1016/B978-0-08-095975-7.00315-6

Wilson, J. T. (1965). A new class of faults and their bearing on continental drift. *Nature*, **207**, 343-347.

Workman, R. K. & Hart, S. R. (2005). Major and trace element composition of the depleted MORB mantle (DMM). *Earth and Planetary Science Letters*, **231**, 53–72, doi: 10.1016/j.epsl.2004.12.005.

Zellmer, G. F., Sakamoto, N., Matsuda, N., Iizuka, Y., Moebis, A. & Yurimoto, H. (2016). On progress and rate of the peritectic reaction Fo + SiO_2 → En in natural andesitic arc magmas. *Geochimica et Cosmochimica Acta*, **185**, 383-393, doi : 10.1016/j.gca.2016.01.005.

Zhang, W. Q., Liu, C. Z., & Dick, H. J. B. (2020). Evidence for multi-stage melt transport in the lower ocean crust: Atlantis Bank gabbroic massif (IODP Hole U1473A, SW Indian Ridge). *Journal of Petrology*, **61**, egaa082, doi: 10.1093/petrology/egaa082.

Zhang, W. Q., Dick, H. J. B., Liu, C. Z., Lin Y. Z. & Angeloni, L. M. (2021). MORB melt transport through Atlantis Bank oceanic batholith (SW Indian Ridge). *Journal of Petrology*, **62**, egab034, doi: 10.1093/petrology/egab034.

FIGURE CAPTIONS

Figure 1: a) Bathymetric map of the Doldrums Megatransform System, combining the data acquired during expedition S45 (see Skolotnev *et al.*, 2020) and the GEBCO bathymetric dataset. Black lines delineate the Mid-Atlantic Ridge (MAR) and the Intra-Transform Ridge (ITR) segments, whereas the white lines highlight the active portions of the transform faults (annotated from 1 to 5). The inset map indicates the location of the studied area in the equatorial Mid-Atlantic Ridge; b) Detailed bathymetric map of the ITR-1. The location of the sampled dredges is indicated by white dots and the proportion of sampled lithologies are represented by pie charts.

Figure 2: a) Detailed bathymetric map of the Peyve Seamount. The locations of the bathymetric profiles A-B and C-D are represented by white lines; b) Profile A-B across the ridge valley and along the Peyve Seamount; c) Profile C-D across the Peyve Seamount and the Vernadsky transform valley; d) Three-dimensional rendering of the bathymetry of Seamount Peyve and associated dredge deployment. The colour scale is the same as the bathymetric map; e) Pie diagrams representing the proportion of all the gabbroic lithotype recovered in the ITR-1 domain and on the Seamount Peyve, redrawn after Skolotnev *et al.* (2020).

Figure 3: Representative hand sample photographs. The location and name of the thin sections realized in these samples is indicated by a red box, which is 4 cm in length; a) Olivine gabbro S45-7-2; b) Gabbro S45-7-1; c) Gabbronorite S45-7-4; d) Oxide gabbronorite S45-7-8; e) Oxide gabbro S45-7-6.

Figure 4: Representative photomicrographs of the olivine gabbros and gabbros sampled at Seamount Peyve. The textures are shown in nicols-parallel and crossed-nicols in the left and right column, respectively; a) Olivine gabbro S45-7-2; b) Olivine gabbro S45-7-7; c) Gabbro S45-7-1B. PL = Plane-polarized light; XPL = Crossed-nicols polarized light.

Figure 5: Representative photomicrographs of the orthopyroxene- and oxide-bearing gabbros sampled at Seamount Peyve. The textures are shown in nicols-parallel and crossed-nicols in the left and right column, respectively; a) Gabbronorite S45-7-4B; b) Oxide gabbronorite S45-7-8; c) Oxide gabbro S45-7-6B; d) Oxide gabbro S45-7-6A. PL = Plane-polarized light; XPL = Crossed-nicols polarized light.

Figure 6: Bulk-rock compositions of the different gabbroic lithologies recovered in the studied area. The composition of bulk Seamount Peyve has been calculated as the weighted average of all recovered samples. The compositions of gabbroic rocks recovered at the Atlantis Massif (after Godard *et al.*, 2009) and Atlantis Bank (after Dick *et al.*, 2000) are represented for comparison; a) Mg-number (100x cationic Mg/(Mg+Fe) mol%) vs Ca-number (100x cationic Ca/(Ca+Na) mol%); b) MgO (wt%) vs FeO (wt%). The compositional field of Mid-Atlantic Ridge peridotites is after Godard *et al.* (2009).

Figure 7: Bulk-rock compositions of the different gabbroic lithologies recovered in the studied area. The compositions of gabbroic rocks recovered at the Atlantis Massif (after Godard *et al.*, 2009) and Atlantis Bank (after Dick *et al.*, 2000) are represented for comparison; MgO content (wt%) vs a) SiO_2 (wt%); b) CaO (wt%); c) Al_2O_3 (wt%); d) TiO_2 (wt%); Na_2O (wt%); CaO/Al_2O_3.

Figure 8: Bulk-rock trace element compositions of the different gabbroic lithologies recovered in the studied area; a) C1-chondrite normalized REE patterns of olivine gabbros, gabbros and oxide

gabbros; b) C1-chondrite normalized REE patterns of gabbronorites and dolerites; c) Primitive Mantle-normalized trace element pattern of olivine gabbros, gabbros and oxide gabbros; d) Primitive Mantle-normalized trace element pattern of gabbronorites and dolerites. Normalization values after Sun and McDonough (1989).

Figure 9: Mineral major element compositions within the different gabbroic lithologies recovered in the studied area. The compositions of gabbroic rocks recovered at the Atlantis Massif (after Miller *et al.*, 2009) and Atlantis Bank (after Dick *et al.*, 2002) are represented for comparison; a) Clinopyroxene Mg-number vs Al_2O_3; b) Clinopyroxene Mg-number vs TiO_2; c) Mg-number in clinopyroxene vs anorthite content in plagioclase; d) Plagioclase anorthite content vs K_2O; e) Orthopyroxene Mg-number vs Al_2O_3; f) Orthopyroxene Mg-number vs TiO_2.

Figure 10: Mineral trace element compositions within the different gabbroic lithologies recovered in the studied area; C1-chondrite normalized REE patterns and Primitive Mantle-normalized trace element patterns of a-b) Clinopyroxene; c-d) Plagioclase; e-f) Orthopyroxene; g-h) Amphibole. Normalization values after Sun and McDonough (1989).

Figure 11: Representative sketch of the inferred process of lateral differentiation, resulting from the reduced melt productivity in the vicinity of the transform fault. The red box indicates the geological setting of the sketch in Figure 16.

Figure 12: Primitive Mantle-normalized trace element patterns of the melts computed in equilibrium with clinopyroxene from: a) Olivine gabbros, Gabbros and Oxide gabbros; b) Gabbronorites. The trace element patterns of primitive N-MORB melts (after Workman and Hart, 2005) and the basalts sampled at the Seamount Peyve are plotted for comparison. Normalization values are after Sun and McDonough (1989) and the compilation of partition coefficients used for calculating the equilibrium melts is after Basch *et al.* (2018).

Figure 13: Modal contents (vol%) of the cumulate gabbro formed during fractional crystallization of an evolved melt, involving the assimilation of various quantities of a primitive crystal mush (10 vol% olivine, 50 vol% plagioclase, 40 vol% clinopyroxene). The composition of the basalt S45-07-173 has been selected as the starting melt composition. Models were computed using the MELTS thermodynamic software (Ghiorso and Sack, 1995). The different models assume a) Fractional Crystallization (FC); b) FC and concomitant assimilation of 0.5g/°C of cooling; c) FC and concomitant assimilation of 1g/°C of cooling; d) FC and concomitant assimilation of 1.5g/°C of cooling; e) FC and concomitant assimilation of 2g/°C of cooling. The yellow field highlights the appearance of orthopyroxene in the fractionated cumulate gabbro.

Figure 14: Clinopyroxene Y_N vs La_N/Sm_N. Compositional trends represent clinopyroxenes computed in equilibrium with melts residual after the process of Assimilation-Fractional Crystallization (AFC models, using the equation from DePaolo, 1981). Ma/Mc ranges from 0 to 0.9. Each tick along the compositional trends represents a decrease in residual melt mass of 5 vol%. Oxide gabbronorites sampled at the Atlantis Bank are shown for comparison (after Zhang *et al.*, 2020). Normalization values are after Sun and McDonough (1989).

Figure 15: Primitive Mantle-normalized trace element patterns of the melt compositions in equilibrium with clinopyroxenes from Figure 14, compared with patterns of Assimilation-Fractional Crystallization (after De Paolo, 1981) of a basaltic parental composition (S45-7-180) assimilating a primitive crystal mush (10 vol% olivine, 40 vol% clinopyroxene, 50 vol% plagioclase) at variable ratios mass assimilated/mass crystallized; a) Model computed at low assimilated mass (Ma/Mc =

0.3) to reproduce the compositions of the oxide gabbros; b) Model computed at high assimilated mass (Ma/Mc = 0.8) to reproduce the compositions of the gabbronorites. Melt fraction decreases from 100% to 5% of the initial melt mass. Mineral/melt partition coefficients are after Basch *et al.* (2018) and normalization values are after Sun and McDonough (1989).

Figure 16: a) Close-up of the magmatic processes occurring in the vicinity of a cold ridge-transform intersection. A lens of primitive gabbroic crystal mush is invaded by the evolved melts percolating laterally from the central portion of the ridge segment. Reaction between the primitive crystal mush and the evolved melt leads to partial assimilation of the gabbroic mush and to the process modeled in Figures 13, 14 and 15; b) Detail of the local melt hybridization, leading to the formation of replacive lithologies ranging from oxide gabbros to oxide gabbronorites and gabbronorites. Each melt percolation channel is characterized by its intrinsic reactivity towards the primitive gabbroic mush, as a function of the melt composition and temperature. Intensive assimilation (Ma/Mc > 0.7) results in the formation of gabbronorites, whereas weaker assimilation (Ma/Mc < 0.5) leads to the formation of oxide gabbros.

Fig. 1.

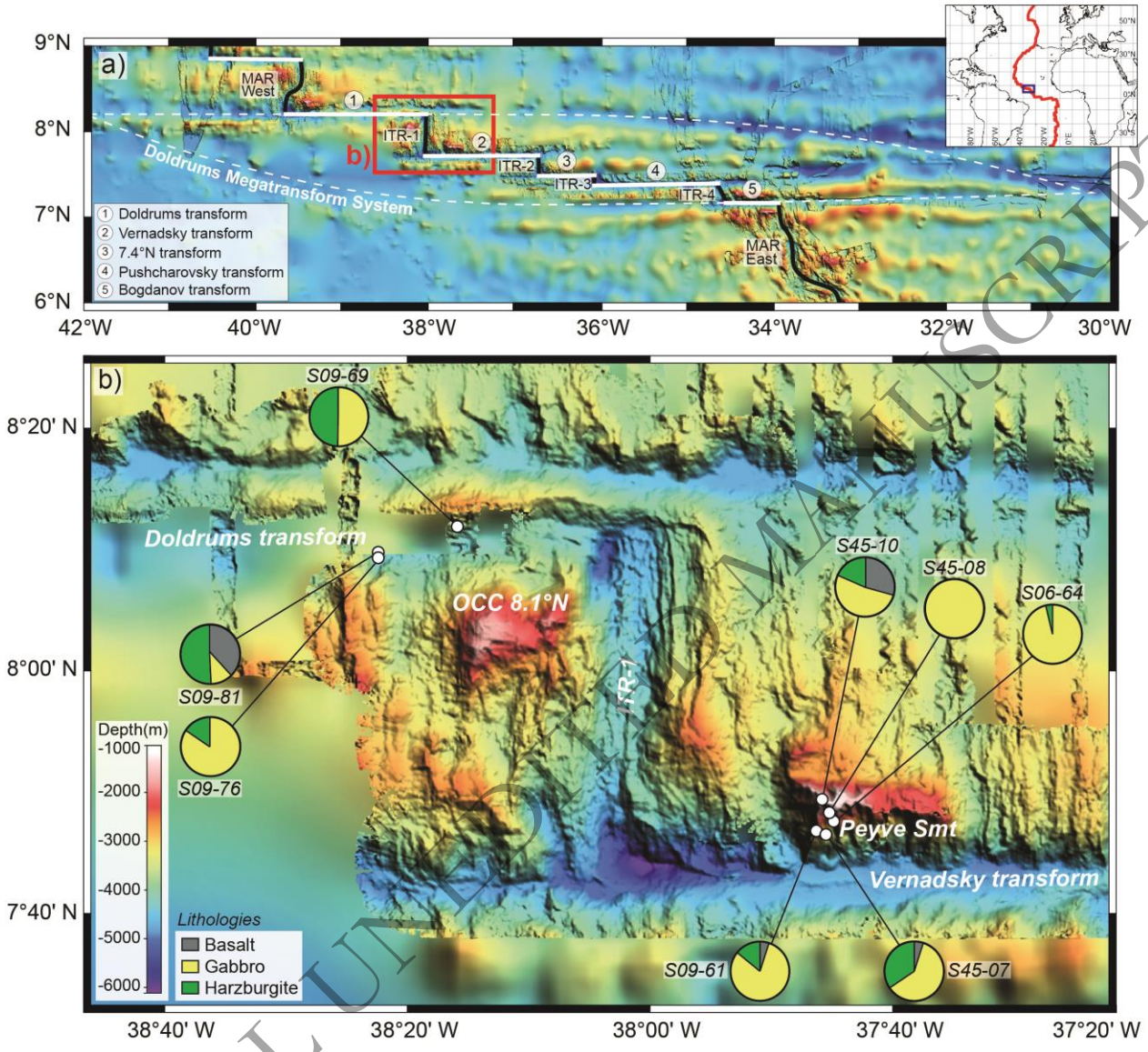

Fig. 2.

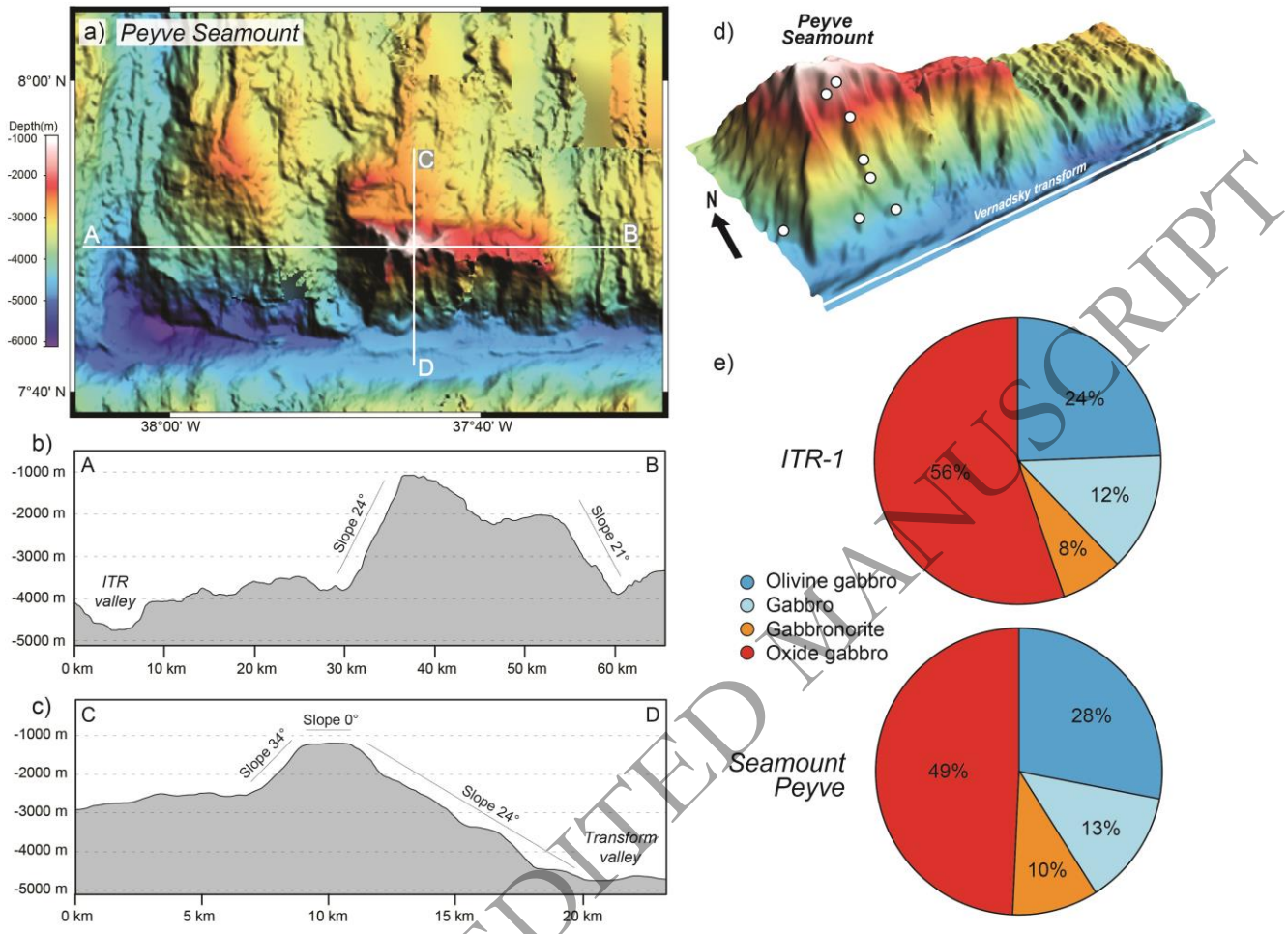

Fig. 3.

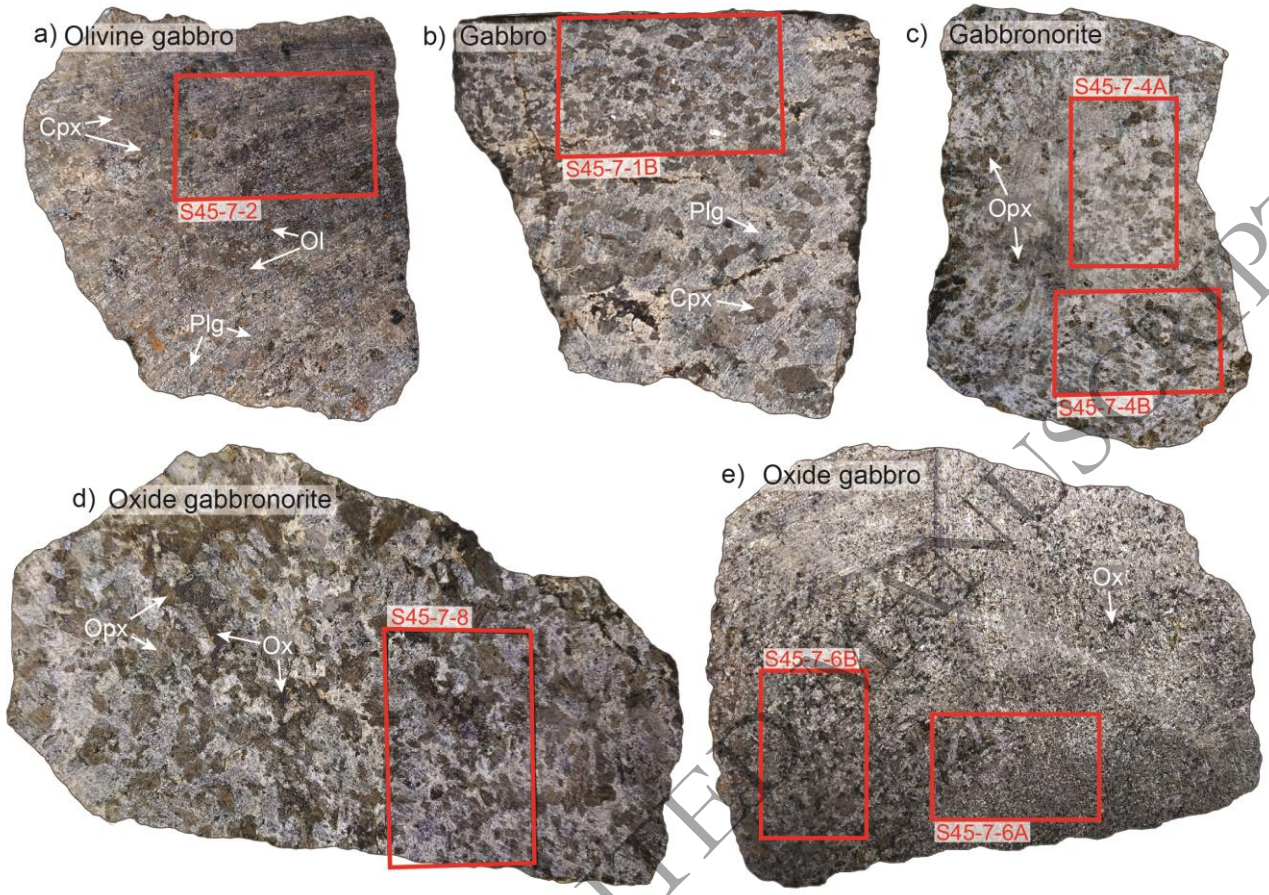

Fig. 4.

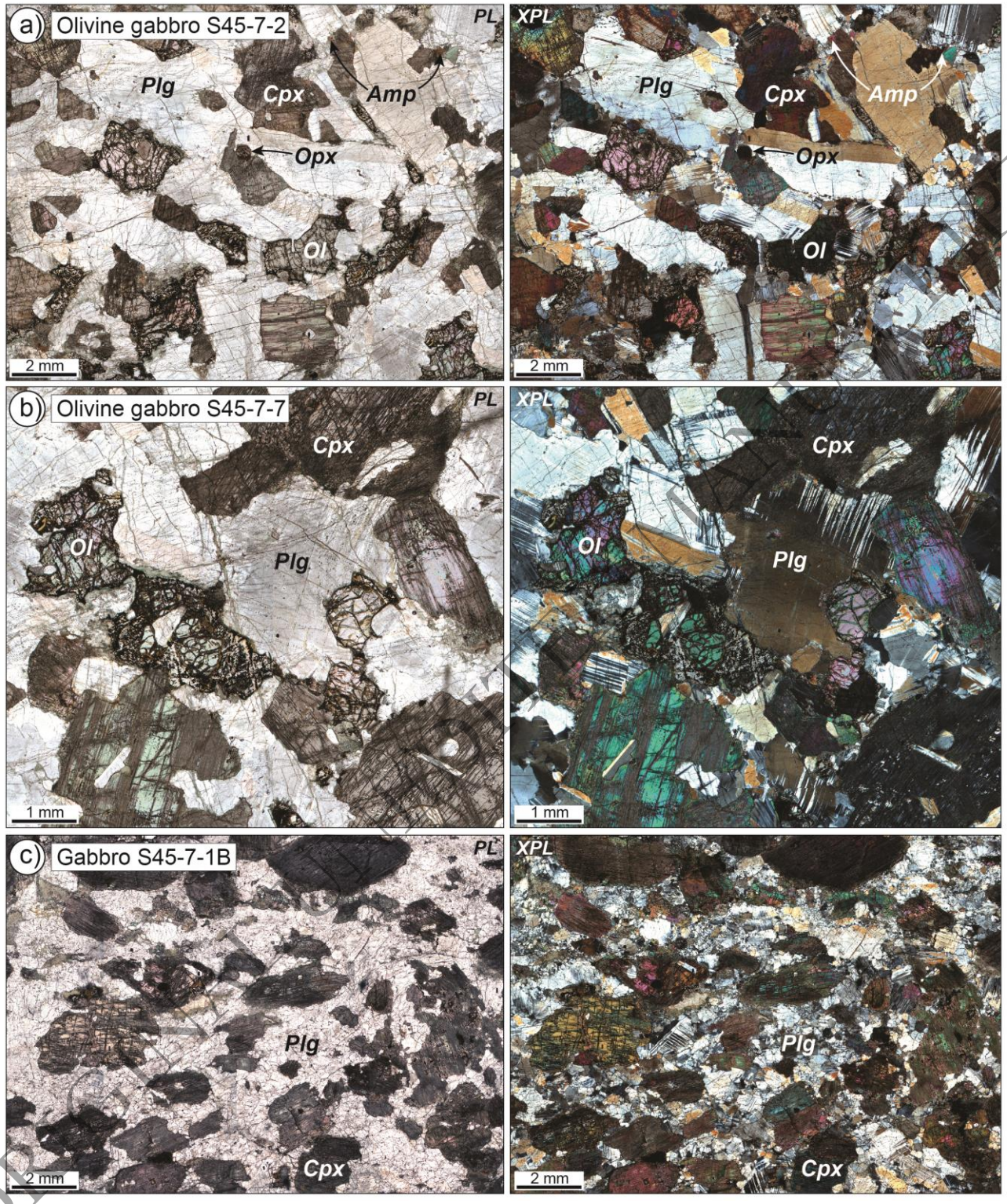

Fig. 5.

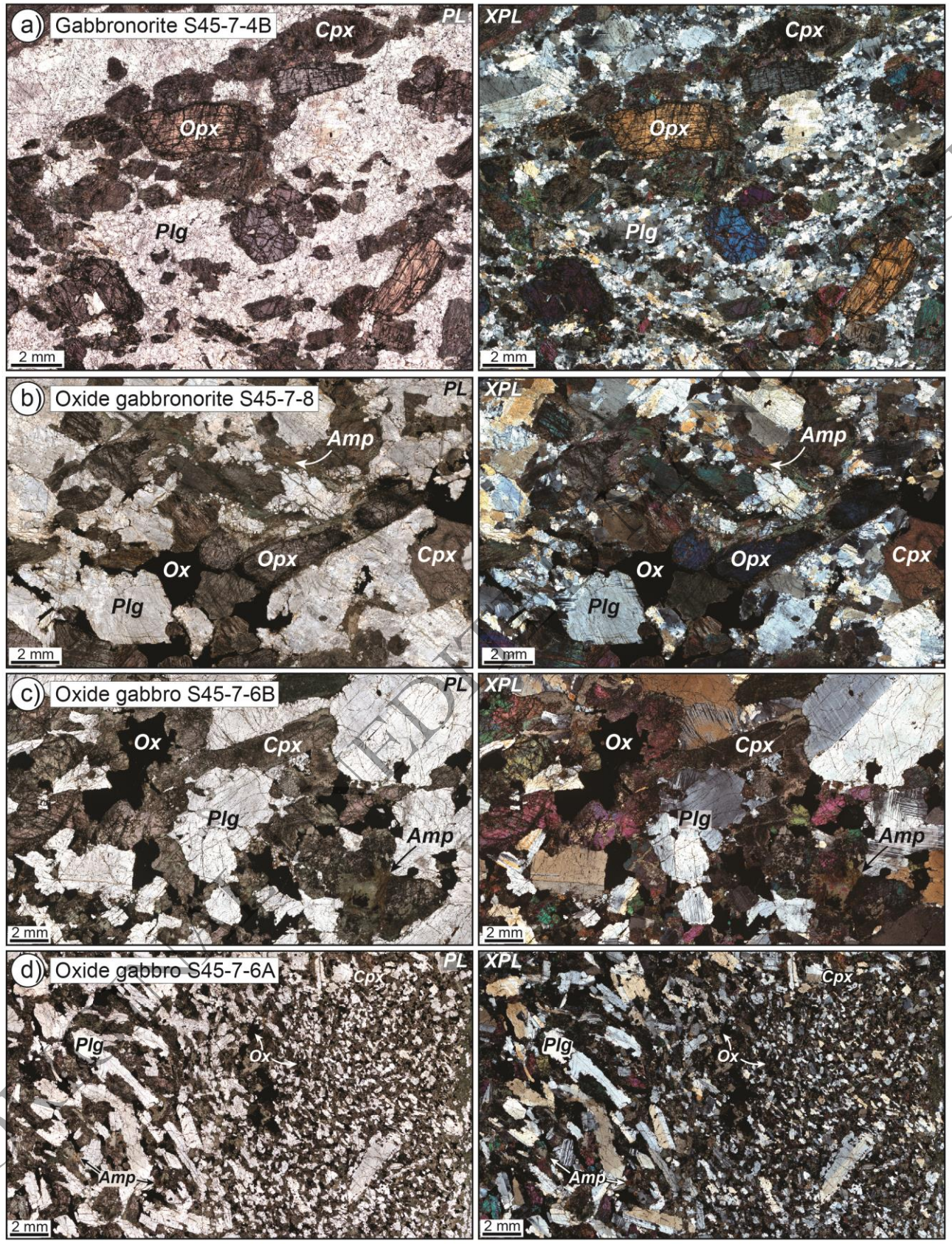

Fig. 6.

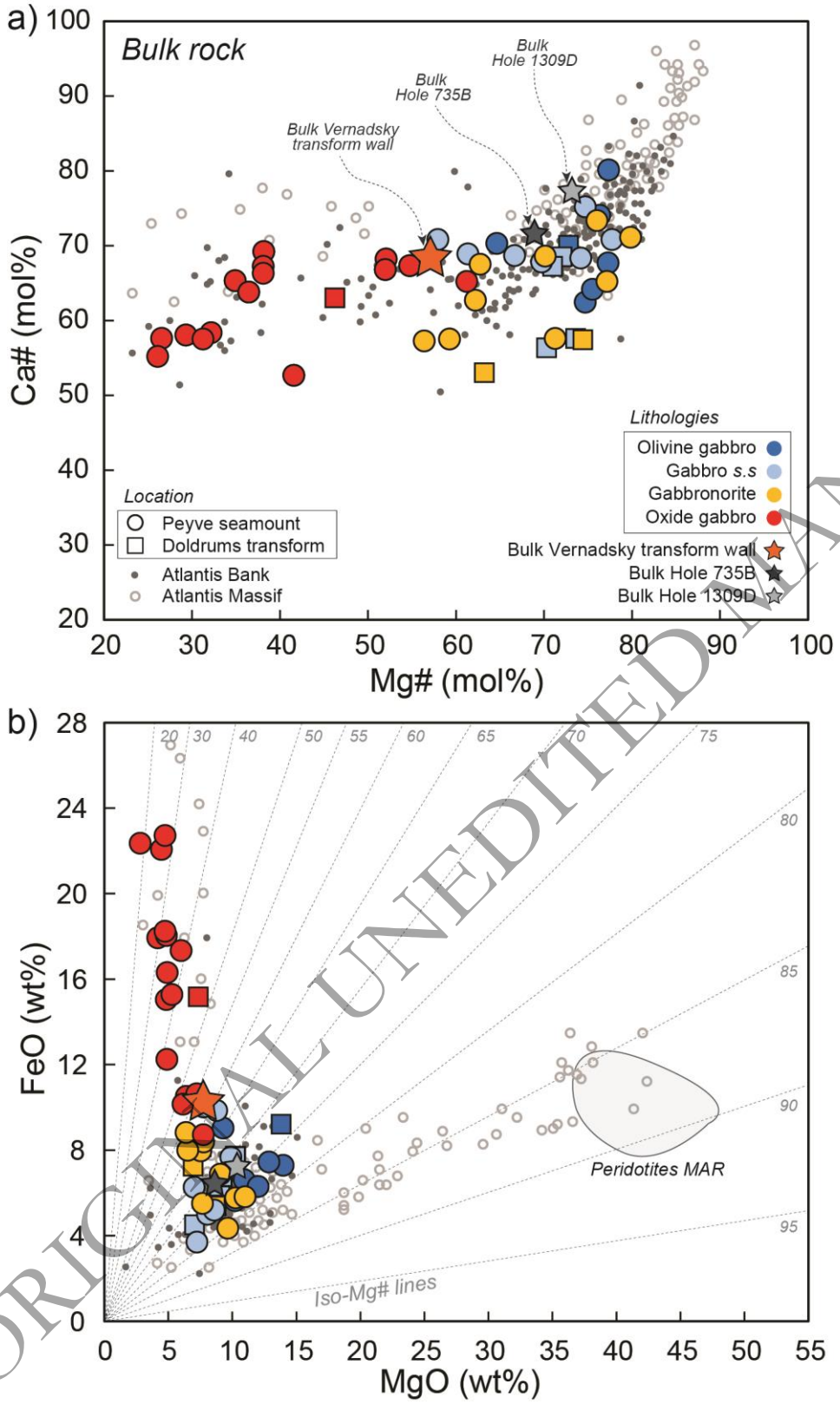

Fig. 7.

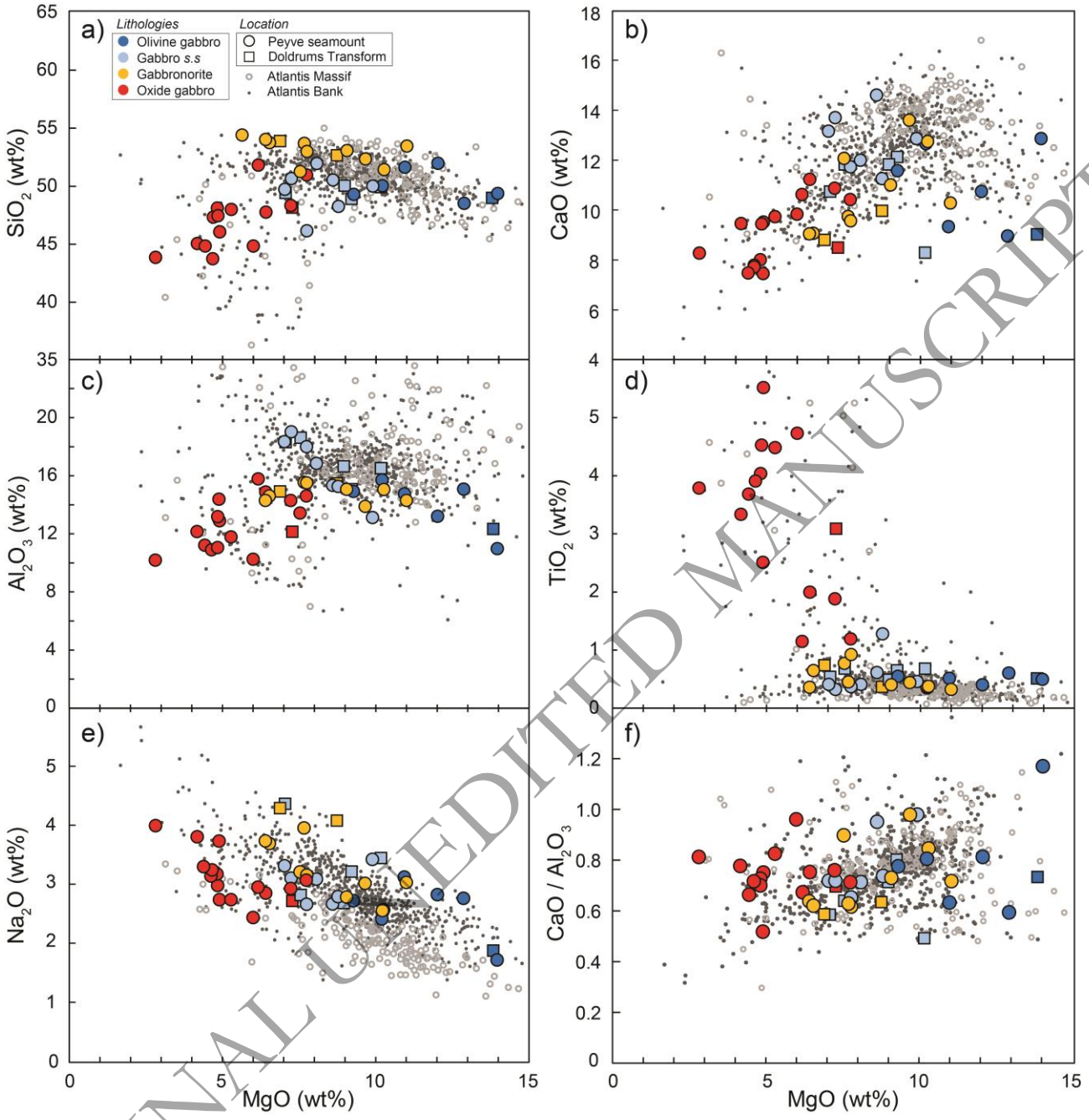

Fig. 8.

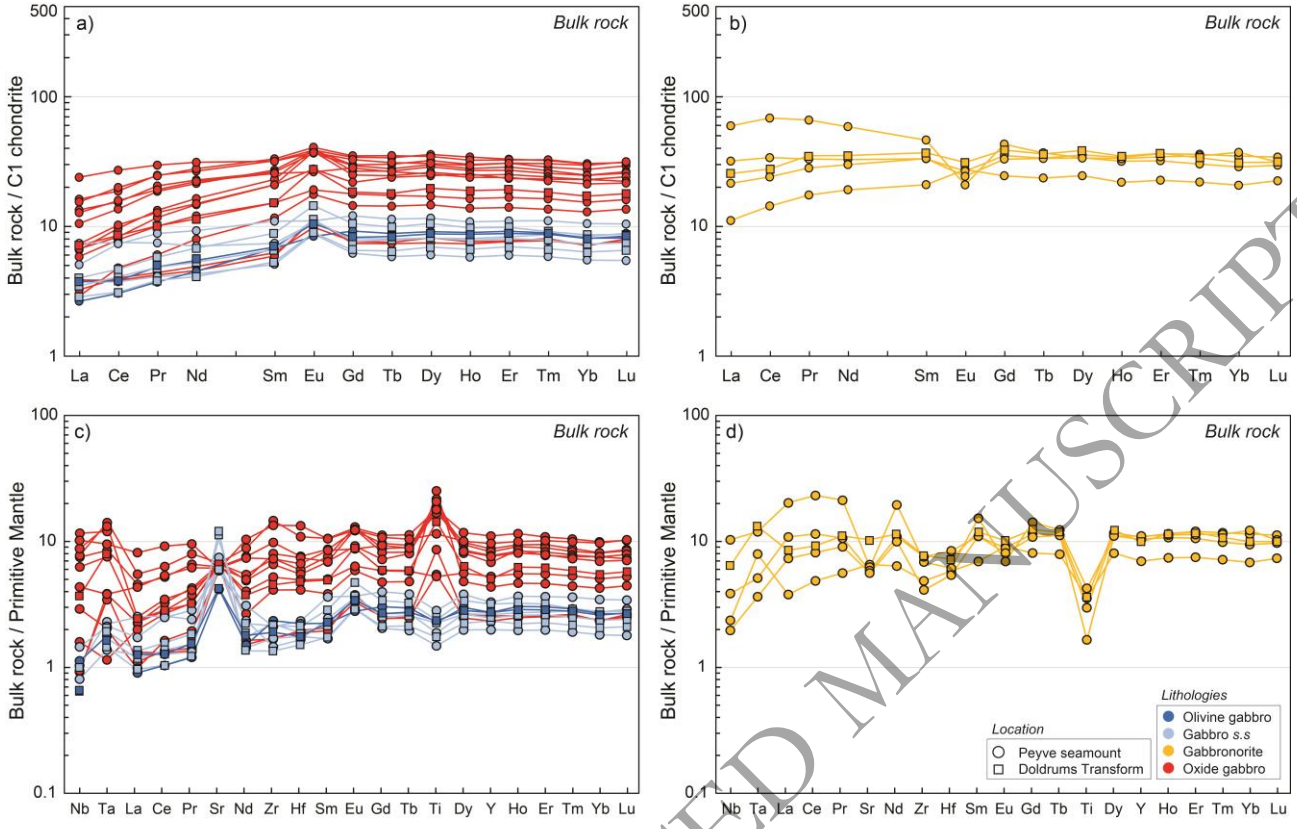

Fig. 9.

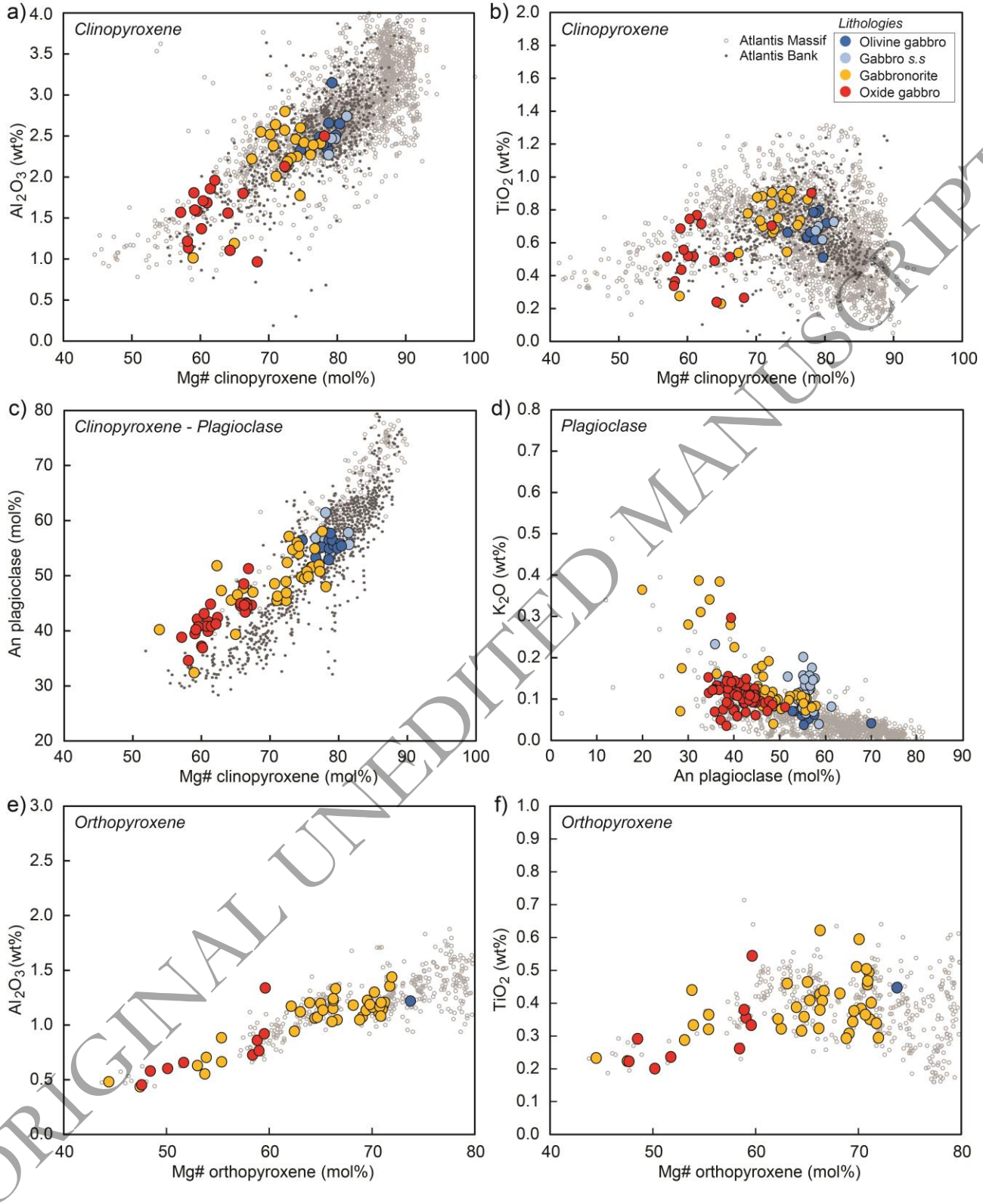

Fig. 10.

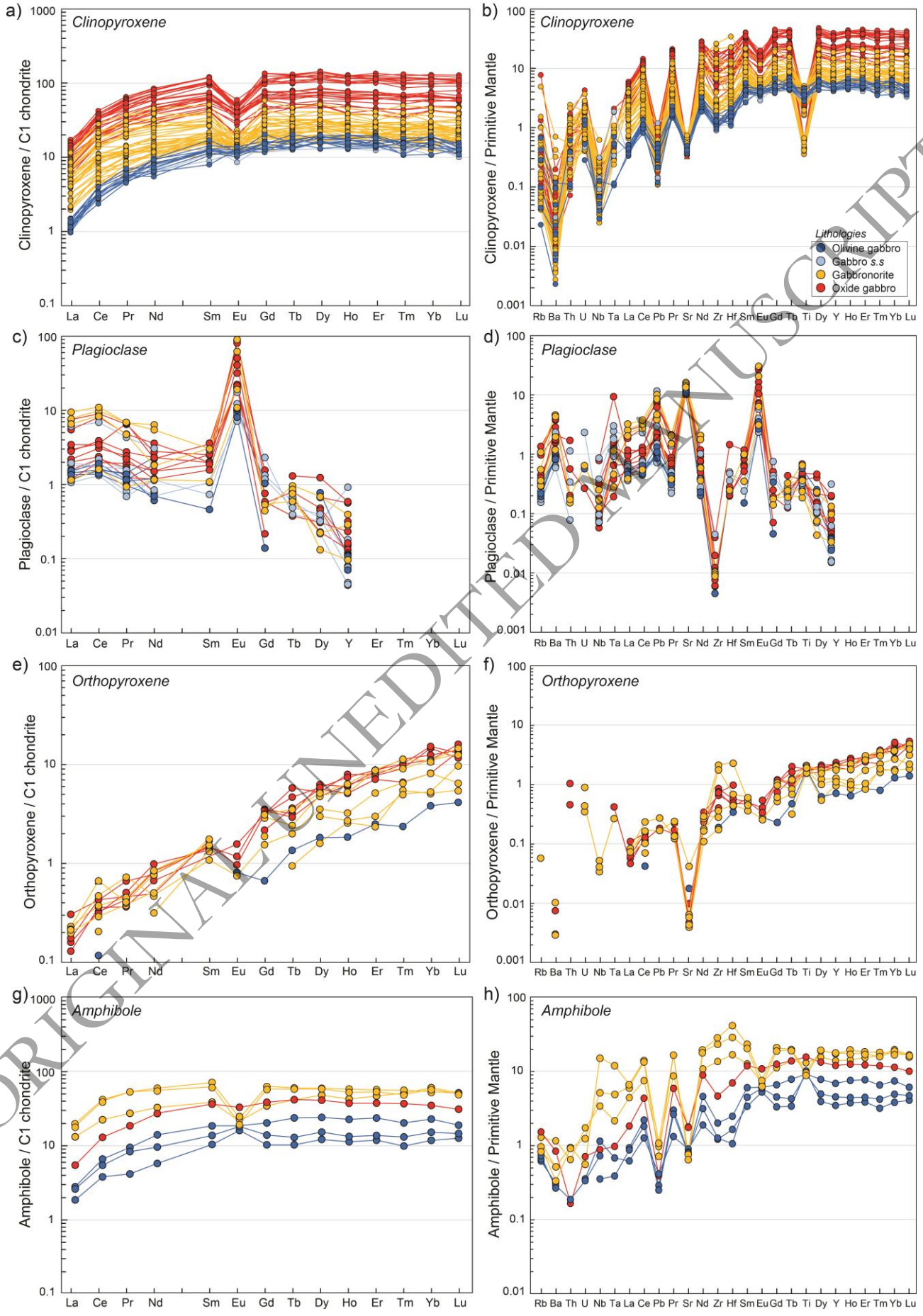

Fig. 11.

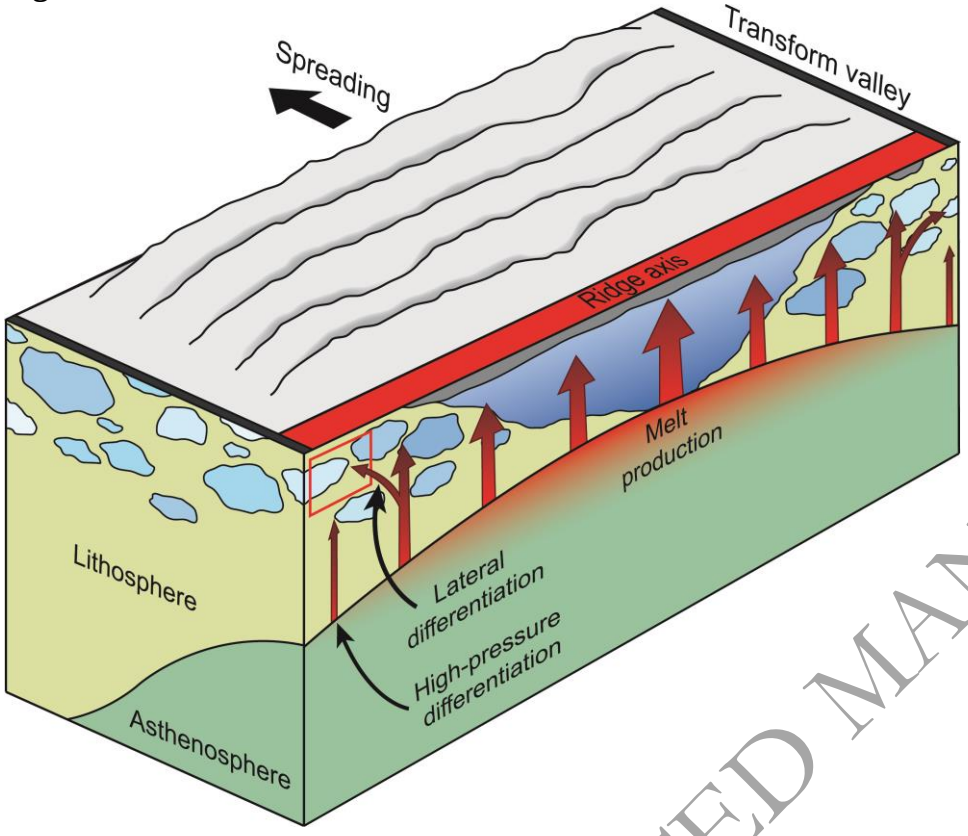

Fig. 12.

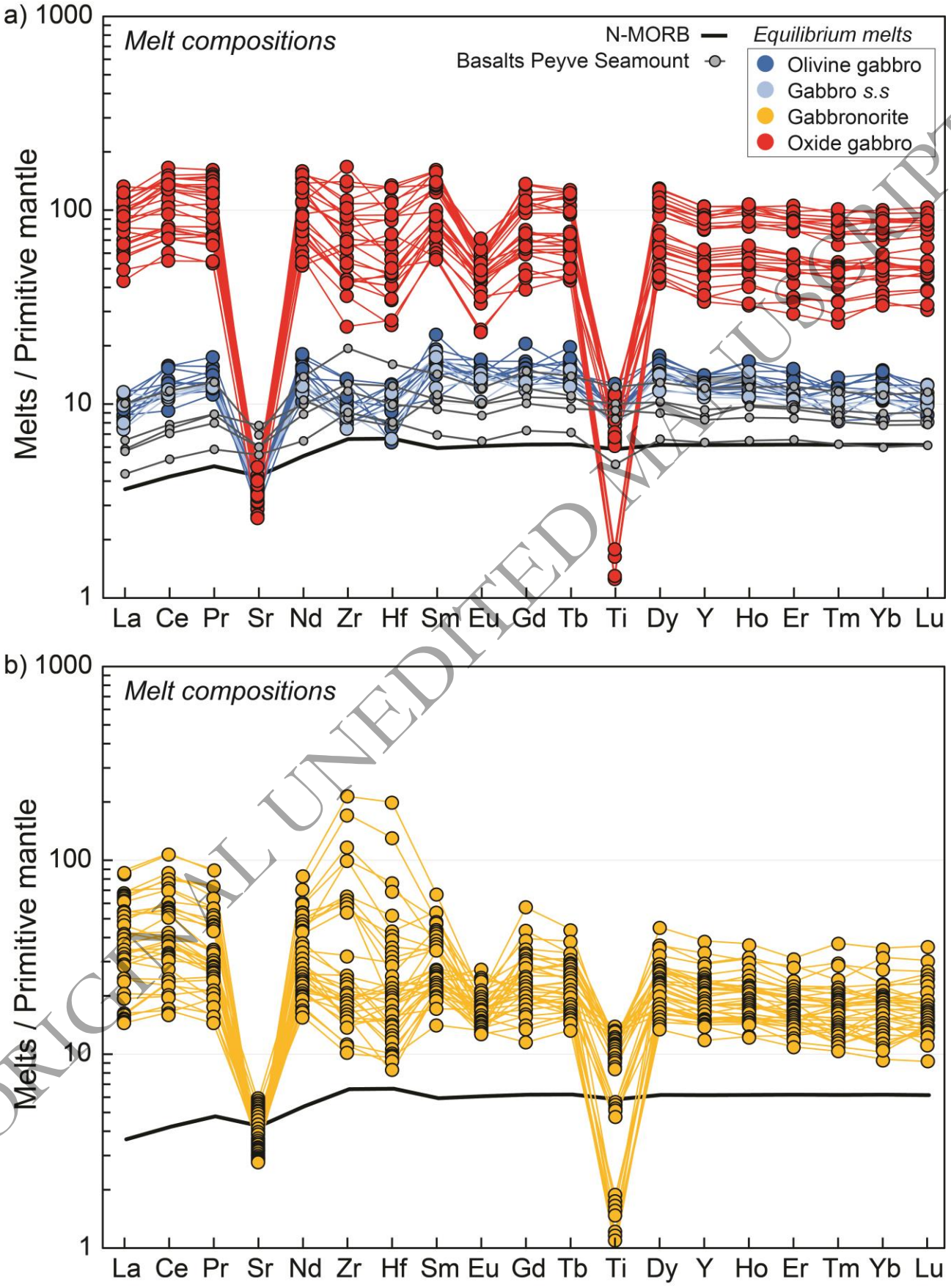

Fig. 13.

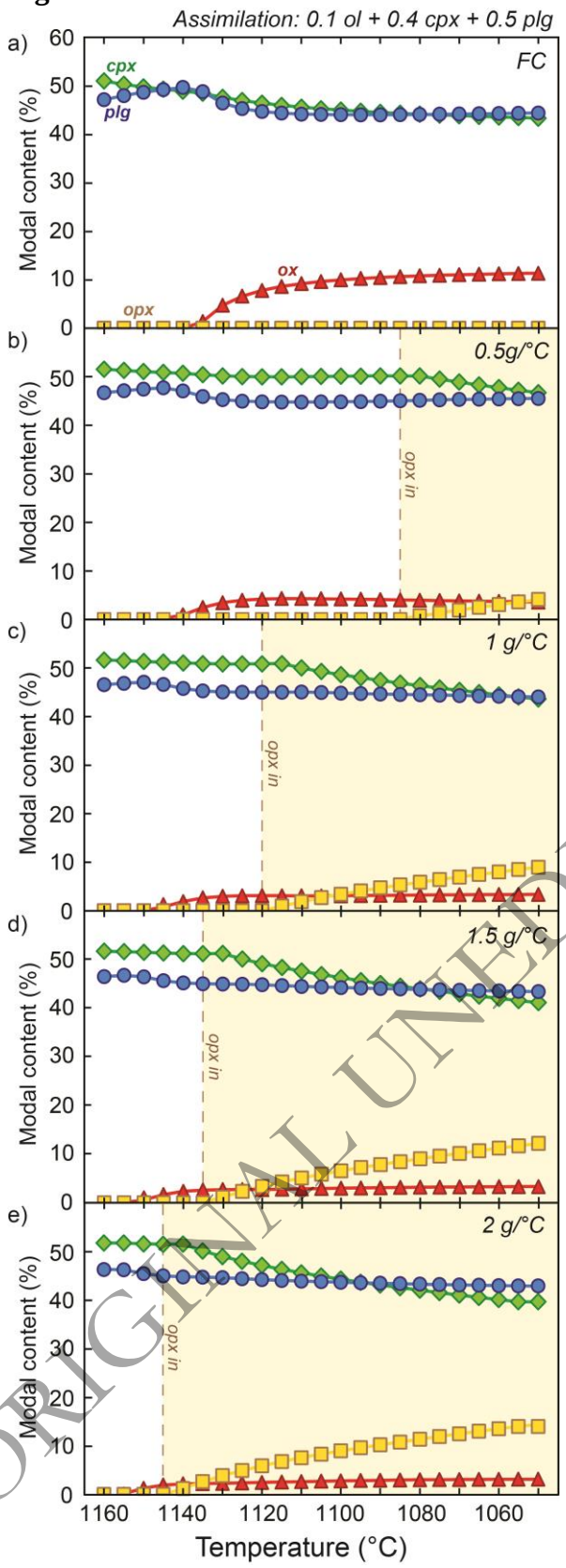

Fig. 14.

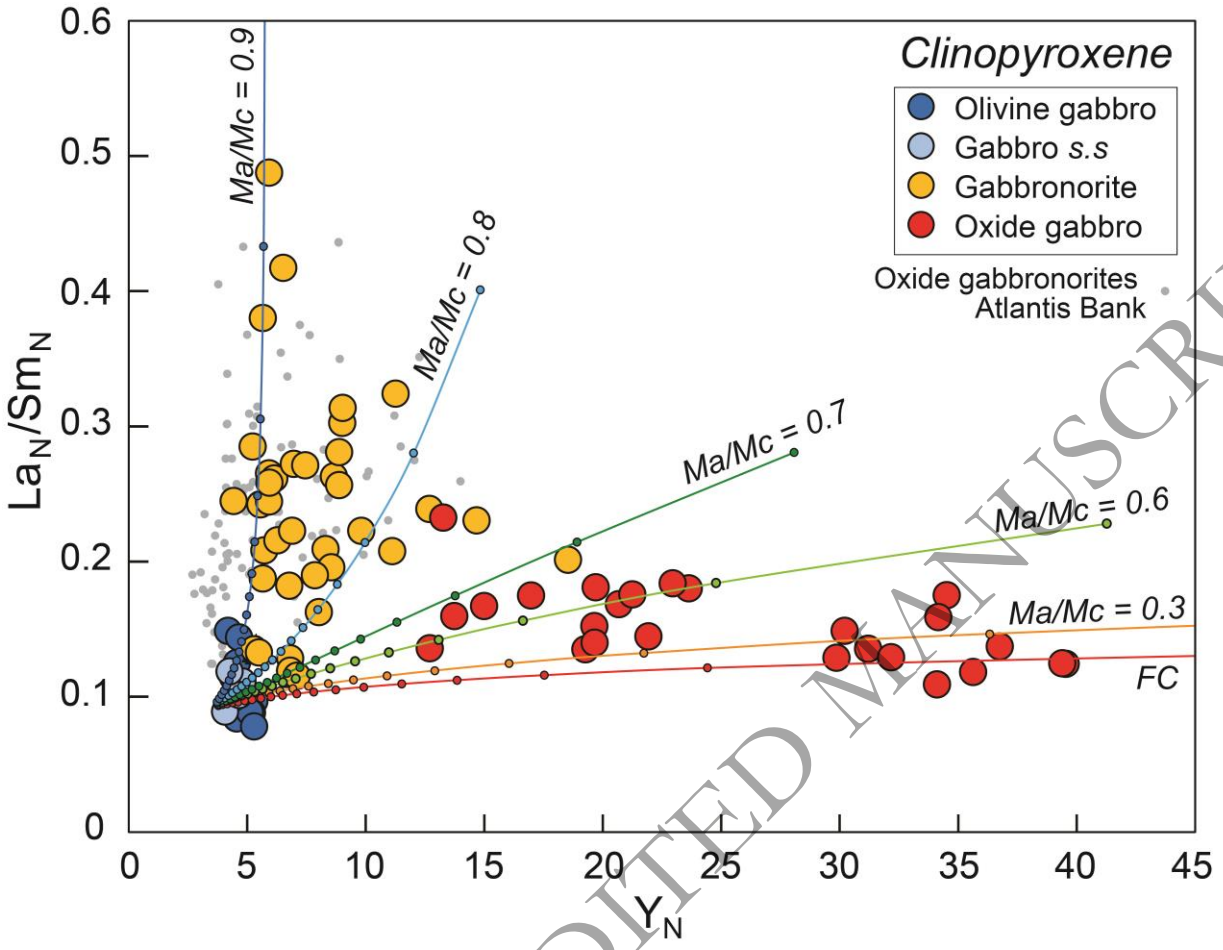

Fig. 15.

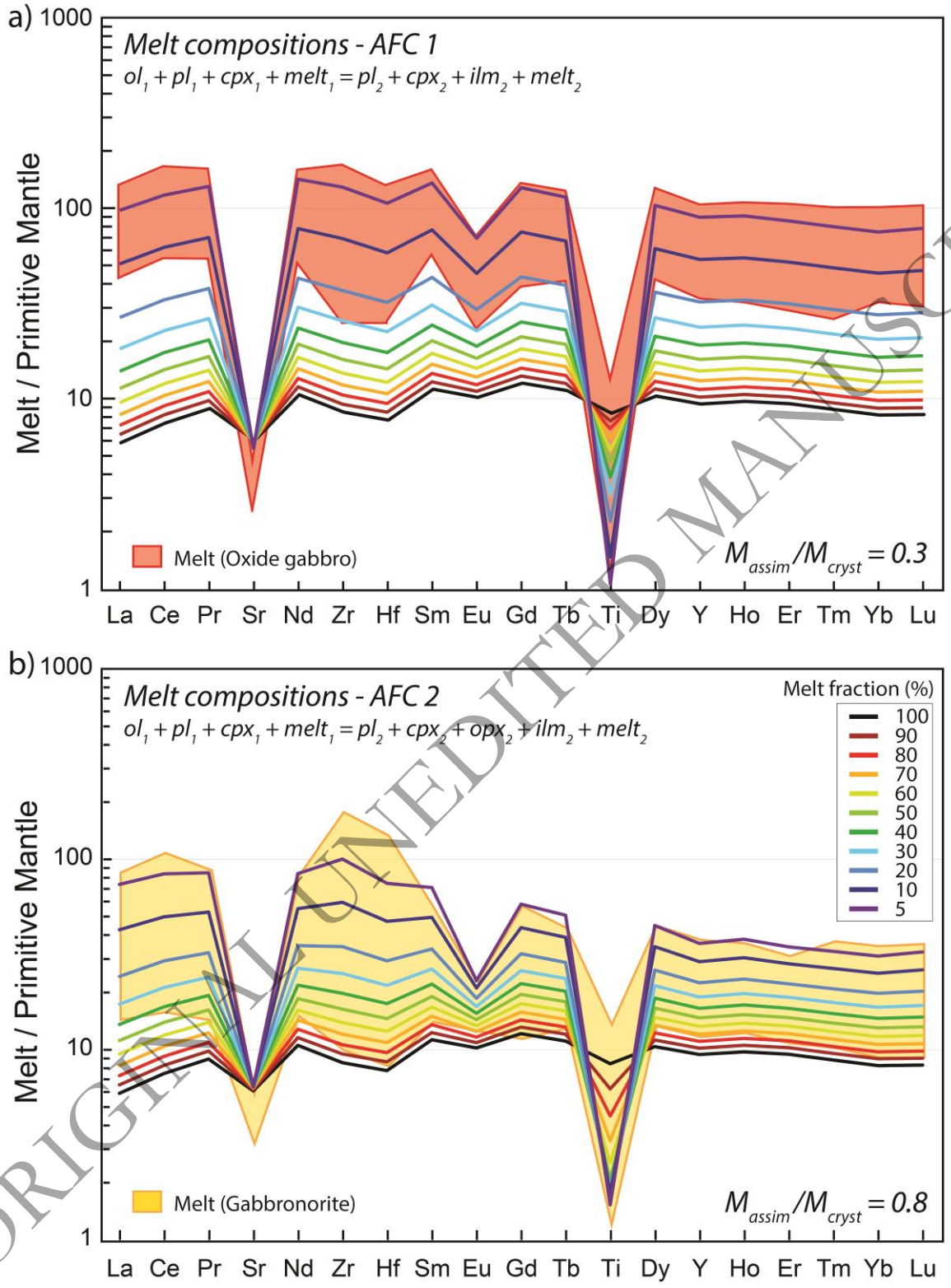

Fig. 16.